Modification of primary carbides in hypereutectic HCCIs

by

Jiaqi Li

A thesis submitted in partial fulfillment of the requirements for the degree of

Master of Science

in

Welding Engineering

Department of Chemical and Materials Engineering
University of Alberta

Abstract

High chromium cast irons (HCCIs) are widely used in oil sands, mining, and manufacturing industrial sectors due to its high resistance to wear, corrosion and corrosive wear. HCCIs are composed of hard carbides and ferrous matrix, resulting in high hardness and reasonably good toughness. In hypereutectic HCCIs, the primary M_7C_3 carbides have greater brittleness compared to the supporting matrix, which may result in detrimental stress at the interface, due to the lattice mismatch increasing the probability of cracking and thus deteriorating the wear resistance. Moreover, since the cracking would be zigzagged at grain boundaries, the expanding of crack would be accelerated with bulky M_7C_3 carbides. Therefore, modification of primary carbides can be an effective method to improve the hypereutectic HCCIs' overall performance.

Core-shell structured carbides have been reported to be beneficial to wear resistance of HCCIs. However, the compositional range of forming such carbides is limited. In the first part of the thesis, thermodynamics analysis was conducted to investigate the conditions for forming core-shell structured carbides and determine the probability of producing such carbides in a wider compositional range via alloying elements. With the guide of thermodynamics calculations, core-shell structured carbides were successfully formed in HCCIs with different carbon concentrations by alloying with boron, confirmed by experiments. For more information, first-principles calculations were conducted to investigate the effect of the B addition on mechanical properties of the $M_{23}C_6$ shell in comparison with those of non-doped $M_{23}C_6$. Also, the reason for B addition promoting the formation of core-shell structured carbides was demonstrated by

interfacial energies of $M_{23}C_6$/Fe and $M_{23}C_6$/M_7C_3 interfaces with or without B, which were achieved using first-principles calculations.

In the second part of the thesis, the effect of alloying elements W and V on mechanical properties of (Fe, Cr, X)$_7$C$_3$ (X=W, V) is investigated. M_7C_3 carbides were tailored by partially substituting the metallic elements with W or V via thermodynamics guidance. A significant correlation between Young's modulus and electron work function of carbides was experimentally observed using multimode atomic force microscope. First-principles calculations were conducted to calculate the modulus and electron work function as a comparison to the experimental data. The atomic bond characteristics in M_7C_3 were investigated. The study correlates the electronic characteristics and mechanical behavior of carbides and guides in designing advanced multi-component M_7C_3 carbides.

Preface

This thesis presents the work supervised by Dr. Dongyang Li. The experiments were conducted in Dr. Dongyang Li's research lab at the University of Alberta.

Chapter 3 represents a manuscript in preparation titled "Promoting the formation of core-shell structured carbides in high-Cr cast irons by boron addition" authored by Jiaqi Li, X. Tang and D. Y. Li. I was responsible for conducting thermodynamics analysis and first-principles calculations, preparing and characterizing the specimens, analyzing the data, and writing the initial draft of the manuscript. All investigations were conducted under Dr. Dongyang Li's supervision.

Chapter 4 is the study as "Tailoring M_7C_3 carbide via electron work function-guided modification" authored by Liqiu Guo, Yunqing Tang, Juan Cui, Jiaqi Li, Jer-Ren Yang and D. Y. Li. I prepared materials, characterized the specimens. The measurement of electron work function, modulus with AFM was obtained by Dr. Liqui Guo. First-principles analysis was conducted by Dr. Yunqing Tang.

Acknowledgments

I sincerely thank Dr. Dongyang Li for inspiring and motivating me during my graduate studies in the University of Alberta. He has been providing me valuable suggestions to tackle the problems I encountered during my research and impressing me with his dedication to science.

I thank all group members for their support and help. My special appreciation is duo to Dr. Liqiu Guo, Dr. Mingyu Wu, Dr. Yunqing Tang and Dr. Kun Wang for their collaboration, advice and help in learning computational methods.

I also would like to thank all the committee members for their input and valuable suggestions on my thesis.

Computational resources provided by Compute Canada is highly appreciated.

Table of Contents

Chapter 3 Promoting the formation of core-shell structured carbides in high-Cr cast irons by boron addition

Chapter 4 Modification on mechanical properties of (Fe, Cr, X)$_7$C$_3$ (X=W, V) in hypereutectic HCCIs...62

List of Figures

x

List of Tables

Chapter 1 Introduction

1.1 Introduction

High chromium cast irons (HCCIs) are widely used in oil sands, mining, manufacturing, and metallurgical machinery industrial sectors due to their high resistance to abrasion, erosion, corrosion and corrosive wear [1, 2]. HCCIs can be hypoeutectic, eutectic and hypereutectic alloys that are all composed of hard carbides and relatively soft but tough ferrous matrix. Carbides such as M_7C_3 and $M_{23}C_6$ withstand the wearing stress while the matrix accommodates deformation and absorbs impact energy with enhanced overall fracture toughness [3, 4]. The alloys containing 12-30wt% Cr and 1.8-3.6wt% C are commonly used [5]. In recent years, HCCIs with higher C and Cr have also attracted interest from material engineers in order to extend applications of HCCIs under various conditions. Increasing the carbon content increases the volume fraction of carbides, leading to elevated resistance to abrasion or sliding wear. Cr helps to stabilize carbides, suppress graphite formation, strengthen the ferrous matrix and form a protective passive film to resist corrosion [4, 6, 7].

However, at high concentrations of carbon added in HCCIs, the microstructure become hypereutectic and contains coarse primary M_7C_3 carbides. The M_7C_3 carbides have greater brittleness compared to the supporting matrix, which may result in detrimental stress at the interface, due to the lattice mismatch increasing the probability of cracking and thus deteriorating the wear resistance [8]. Moreover, since the cracking would be zigzagged at grain boundaries, the expanding of crack would be accelerated with bulky M_7C_3 carbides in hypereutectic HCCIs [8, 9].

One way that has been proven effective in decreasing such interfacial stress and improving the wear resistance of HCCIs is to build core (M_7C_3)-shell ($M_{23}C_6$) structured carbides by in-situ $M_7C_3 \rightarrow M_{23}C_6$ carbide transformation [5, 7, 10, 11]. Tang et al. [7] investigated HCCIs having 45wt% Cr and observed that Fe-45wt%Cr-4wt%C HCCI had the core-shell structured carbides, which exhibited higher resistance to wear and erosion than its family alloys without the core-shell structured carbides. Wear modeling and related finite element analysis [12] demonstrate that the shell $M_{23}C_6$ in the core (M_7C_3)-shell ($M_{23}C_6$) structured carbides, whose hardness is between those of the core (M_7C_3) and the matrix, generates a transitional layer at the M_7C_3/matrix interface and helps reduce the interfacial stress, leading to increased resistance to wear. However, the reason why the core-shell structured carbides are only observed in Fe-45wt%Cr-4wt%C HCCIs remains unclear. Hence, thermodynamics-kinetics analysis has been performed in order to investigate the compositional effect on the formation of core-shell structured carbides in Fe-Cr-C alloys [13]. The compositional range and driving force for the formation of core-shell structured carbides is preliminarily discussed and a prediction of forming the core-shell structured carbides with wider carbon concentration range by adding alloying elements could be achieved by means of a thermodynamics technique. Boron could be a suitable alloying element which is often used to modify the microstructure and carbides for cast irons and hardfacing alloys as well as form borides for higher hardness and wear resistance [14-18]. It has been determined that boron can reside on carbon sublattice sites to form complex compounds and facilitate nucleation of $M_{23}(C, B)_6$ [19]. First-principles calculations on quaternary (Fe, Cr)$_{23}$(C, B)$_6$ show that regardless of the Cr/Fe ratio, the stability of (Fe, Cr)$_{23}$(C, B)$_6$ increases with increasing boron concentration [20]. Previous

studies have demonstrated that when B/(B+C) ratio is over 0.75, M_2B becomes more dominant, while $M_{23}(C, B)_6$ can be stabilized when B/(B+C) ratio is below 0.75 [21, 22]. Thus, utilizing boron in HCCIs could be a promising way to generate desired core-shell structured carbides.

Another way to enhance the wear resistance of HCCIs is to modify the mechanical properties of the primary M_7C_3 carbides by doping with foreign elements. Recent studies [23, 24] have demonstrated that some strong carbide-forming elements such as W and Mo, as well as elements that can substitute carbon like B, can dissolve in the M_7C_3 carbide and change its mechanical properties. Either the strength of M_7C_3 can be improved without much decrease of toughness, or the ductility of M_7C_3 can be elevated with a small loss of strength. Both situations may result in enhanced wear resistance of HCCIs. However, it is unclear how to predict the effect of alloying elements on the mechanical properties of M_7C_3. A study [6] has shown that among (Fe, Cr)$_7C_3$ carbides with various Cr/Fe ratios, the electron work function (EWF) of (Fe, Cr)$_7C_3$ is correlated to their elastic moduli. Also, the correlation between EWF and mechanical properties of metals such as hardness, elastic moduli and fracture toughness were previously investigated [25-27]. Hence, EWF could help develop a criterion for selecting alloying elements to modify the mechanical properties of M_7C_3.

In this thesis research, the primary M_7C_3 carbides were modified in two ways for improved properties. One was to form the core-shell structured carbides with boron addition in order to produce such carbides over a wider carbon range. Relevant thermodynamics analysis was conducted to determine the chemical composition of ferrous alloys and the following heat treatment. Experiments were then performed to

validate the calculated results. First-principles calculations were also conducted to investigate how the B addition could influence properties of $M_{23}C_6$ carbides, including its mechanical strength and interfacial bonding with both the matrix and the core M_7C_3 carbide. The other was to dope tungsten and vanadium in M_7C_3 and investigate their effects on the mechanical properties of M_7C_3. Samples were made and characterized using atomic force microscopy. First-principles calculations were conducted to calculate the mechanical properties and EWF of (Fe, Cr, X)$_7$C$_3$(X=W, V). The correlation of EWF and strength of (Fe, Cr, X)$_7$C$_3$ was analyzed and discussed.

1.2 Literature review

1.2.1 High Chromium Cast Irons (HCCIs)

1.2.1.1 Microstructure of HCCIs

High chromium cast irons can be hypoeutectic, eutectic and hypereutectic alloys consist of proeutectoid and/or eutectic hard carbides and a ductile matrix as shown in Fig.1 [4]. For hypoeutectic alloys, the as-cast microstructure is composed of primary austenite dendrites, eutectic austenite and eutectic M_7C_3 or M_3C carbides. The type of carbide is dependent on the Cr content in the alloy such that usually a low Cr (<12wt%) content can lead to the formation of M_3C eutectic carbides instead of M_7C_3 carbides [28]. While in hypereutectic HCCIs, the as-cast microstructure is primary M_7C_3 carbides and eutectic matrix+ M_7C_3 colonies.
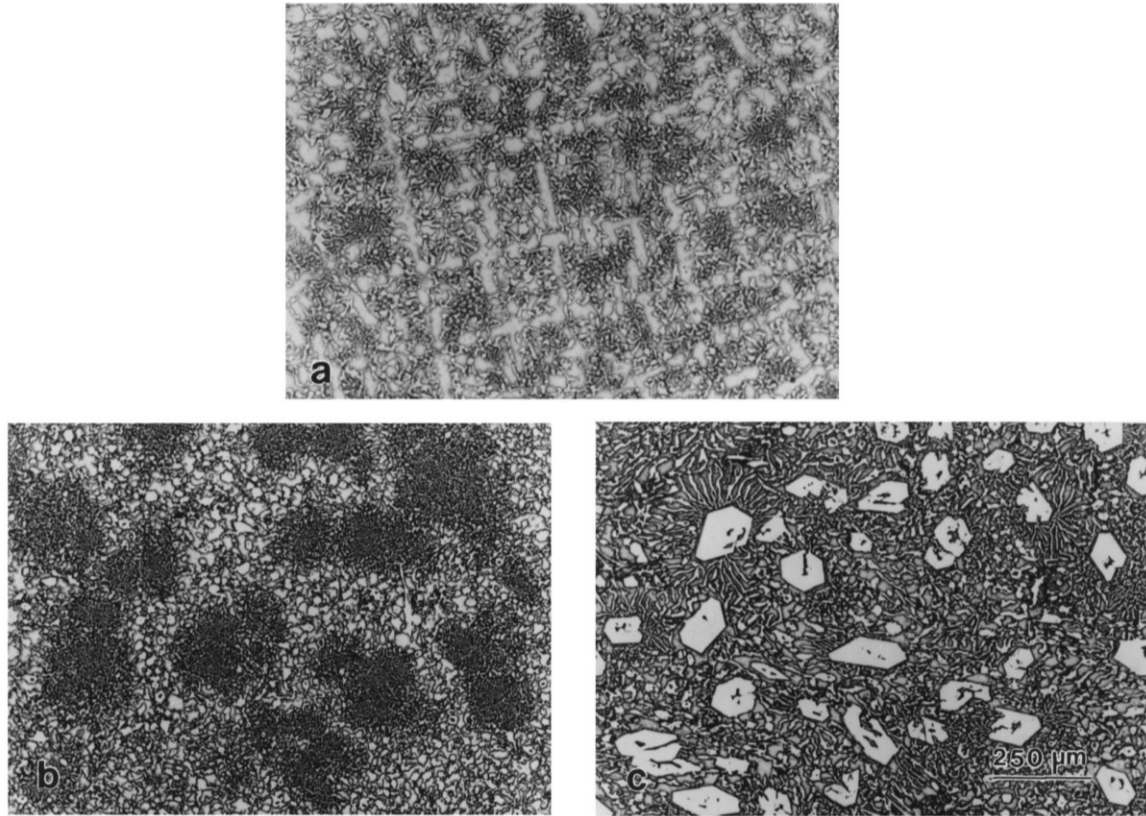
Fig.1 *Optical micrographs of 26Cr cast irons: (a) hypoeutectic, (b) eutectic and (c) hypereutectic [4].*

Moreover, the matrix within high chromium irons varies and influences the mechanical properties of alloys. The matrix is commonly austenite, martensite, or pearlite according to the alloy composition and heat-treating procedure [4]. The matrix is generally austenite which may undergo transformation during the cooling process, which is shown in Fig.2 [29]. According to Fig.2, the transformation of austenite is highly affected by the cooling rate. Rapid cooling can suppress the transformation from austenite to pearlite, and martensite could be the product. Besides rapid cooling, alloying elements such as Ni, Mg and Cu, also suppress the eutectoid transformation of austenite to pearlite. Cr is normally not considered as a pearlite-suppressing element since most of

it resides in carbides. However, when chromium of high content is added to the iron, a fair amount of chromium would be dissolved in the matrix, thus hindering the transformation to pearlite. As for the transformation from austenite to martensite, despite rapid cooling, when secondary carbides are precipitated within the matrix during heat treatment, it may increase the M_s temperature so that austenite could be easier to transform to martensite [30, 31].
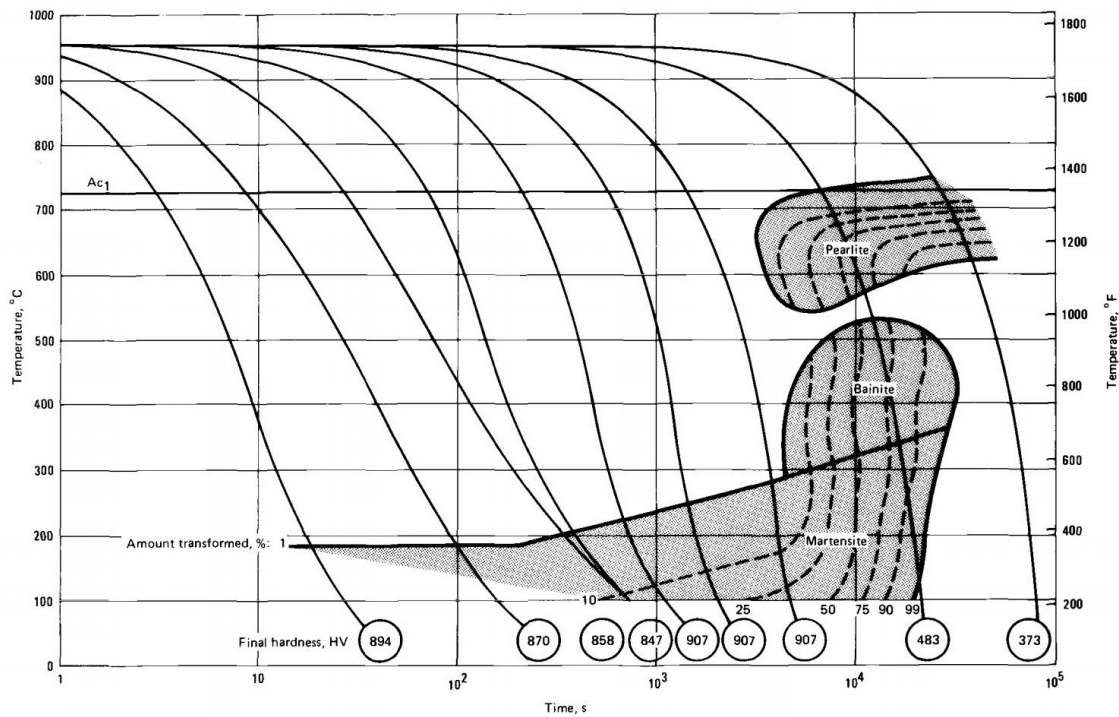
Fig.2 *Continuous-cooling diagram of 2.96C-0.93Si-0.79Mn-17.5Cr-0.98Cu-1.55Mo*

alloy [29].

Since mechanical properties of the matrix can be different when in different phase states, the type of matrix influences the overall performance of cast irons. Martensite has the highest hardness and tensile strength among micro-constituents, which is beneficial to the abrasive resistance; thus martensitic cast irons are commercially attractive [29]. Austenite, one of micro-constituents, although slightly softer than pearlite, may lead to

6

higher wear resistance than pearlite [4]. This happens because pearlite is more difficult than austenite to be deformed due to its lamellar structure. Thus, austenite can better support the carbides and delay their fracture more effectively during the wear process. Also, austenite may transform to martensite under external stress, leading to higher strain-hardening capability and thus further increases the abrasive resistance.

1.2.1.2 Wear resistance of HCCIs

Since HCCIs are effective when used in severe environment that normally includes abrasion, erosion or corrosive erosion, their wear resistance is a vital criterion when evaluating such materials. These properties are dependent on the macrostructure [32-36], the ferrous matrix [37-40] and more importantly, the type, morphology and distribution of hard carbides [32, 33, 37-39].

The type of matrix is an important factor to wear resistance of HCCIs. Compared to lamellar structured pearlite and austenite, martensite which presents the highest hardness among ferrous matrix is more beneficial to the wear resistance.

Since carbides are hard phases in HCCIs, they withstand the wearing forces during wear. Thus, they are considered the predominant constituents. Among the stable M_3C, M_7C_3 and $M_{23}C_6$ carbides, M_7C_3 exhibits the highest hardness which ranges between 1300-1800HV, whereas the hardness of M_3C is 800-1000HV and that of $M_{23}C_6$ is about 1000HV [28]. Therefore, M_7C_3 is the preferential carbide in HCCIs. The effects of orientation and volume fraction of M_7C_3 on wear resistance of HCCIs are described below.

The primary M_7C_3 carbides in cast irons are hexagonal rods, which can be transverse or longitudinal to the wear surface, leading to different wear resistance. The two orientations of M_7C_3 are shown in Fig.3 [41]. Previous studies [41] have presented that the M_7C_3 carbides transverse to the wear surface exhibit higher microhardness and better wear resistance than longitudinal M_7C_3.
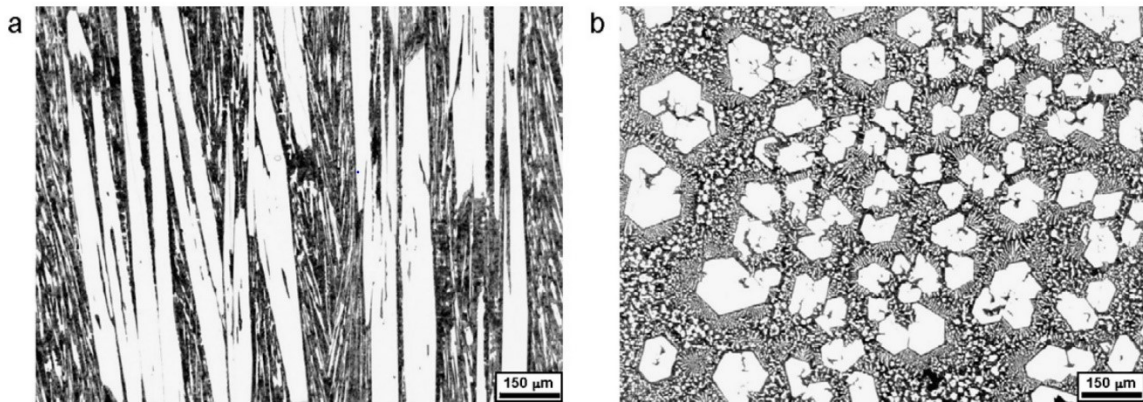
Fig.3 *Optical micrographs of white cast irons with 24.41%Cr showing two orientations of M_7C_3: (a) longitudinal and (b) transverse. [41]*

Abrasive wear occurs when hard asperities sliding against a softer surface or hard particles are introduced to damage the material [42]. The former is called two-body abrasion whereas the latter is called three-body abrasion. Abrasive wear is affected by various factors such as the hardness, toughness and microstructure of materials or the hardness, size and morphology of abrasive particles [32]. In the case of high chromium cast irons, the reinforcing phase, M_7C_3, strongly affects the abrasive wear resistance. The effect of carbides volume fraction (CVF) in high chromium cast irons on three-body abrasion is considered to be related to the hardness of abrasive particles [32]. When abrasive particles are softer than M_7C_3, the wear resistance first increases with CVF,

reaches a maximum at the eutectic composition, then decreases. When CVF is low, the alloy is in a hypoeutectic state. With increasing content of carbon and chromium, CVF increases while the corresponding spacing between carbides in the eutectic colony decreases. As a result, it would be more difficult for the abrasive particles to wear off the softer matrix, hence the abrasion resistance increases with CVF. As the content of carbon increases to a certain level, the microstructure becomes hypereutectic. In this case, bulky primary M_7C_3 would be protruded during wear processes because the matrix is relatively easier to be worn off compared to M_7C_3, especially when abrasive particles are softer than M_7C_3. As a result, spalling and pitting of primary M_7C_3 can be caused, leaving the matrix exposed to the wearing force, resulting in decreased abrasion resistance. When the hardness of abrasive particles is comparable to M_7C_3, the abrasion mechanism is similar to that for hypoeutectic and eutectic alloys. However, the situation is different for hypereutectic cast irons. If the abrasive particles are hard enough to simultaneously wear matrix and carbides, the primary M_7C_3 is surrounded by matrix during the wear process, so that the carbide can be maintained, and drop-off of carbides is rare. Therefore, the abrasion resistance still increases with CVF.

Erosive wear is caused by impact of particles against the surface of materials [43]. The erosive wear rate is influenced by various factors, such as size, morphology of erodent particles, impingement angle and microstructure of the material [44]. In the case of erosive wear of HCCIs, CVF plays an important role [45, 46]. When erodent particles are relatively softer than carbides, such as iron ore and blast furnace sinter, no gross fracture is observed on primary carbides. Thus, carbides can withstand the impact and decrease wear rate as CVF increases. When erodent particles have similar or higher

hardness, compared to that of carbides in HCCIs, such as silicon carbide, cracks readily form on bulky carbides, leading to fracture of carbides, production of large debris, cavity on the matrix and further wear of materials. In other words, a large fraction of carbides may not be beneficial to the erosion resistance of HCCIs.

1.2.2 Improving the mechanical properties of HCCIs

From the above discussion on mechanical properties of HCCIs, carbides play an important role in resisting wear, withstanding the wearing force due to their high strength. However, the carbides may induce cracking and deteriorate the materials when impact forces are involved. Thus, efforts were made to develop techniques for modifying the carbides in order to improve the mechanical properties of HCCIs. Several approaches including forming core-shell structured carbides, refining carbides via alloying elements or doping alloying elements in carbides, have been proven beneficial to mechanical properties of HCCIs and are described below.

1.2.2.1 Core-shell structured carbides

In HCCIs, the carbide may change its structure as $M_3C \rightarrow M_7C_3 \rightarrow M_{23}C_6 \rightarrow M_6C$ [11]. M_3C has an orthorhombic crystal structure, M_7C_3 is a hexagonal closely packed carbide, whereas $M_{23}C_6$ and M_6C are face-centered crystals. Three transformations, $M_3C \rightarrow M_7C_3$, $M_7C_3 \rightarrow M_{23}C_6$ and $M_{23}C_6 \rightarrow M_6C$, are all considered in-situ transformations. The carbides before and after transformation have shown crystal orientation relationships, which were determined by transmission electron microscopy. The misfit of carbides lattices before and after the transformation is small, indicating that the orientation relationship can be easily maintained during the transformation. In the $M_3C \rightarrow M_7C_3$

process, M_7C_3 nucleates at part of the ferrite/M_3C interface, then grows into M_3C. The boundary of M_3C and M_7C_3 is found to be straight and lie along the (0 0 1) plane of the cementite. However, in the process of $M_7C_3 \rightarrow M_{23}C_6$, $M_{23}C_6$ nucleates at the entire interface and grows towards the core of M_7C_3. In the case of $M_{23}C_6 \rightarrow M_6C$, M_6C nucleates not only at the ferrite/$M_{23}C_6$ interface but also inside $M_{23}C_6$, which may be relevant to the planar faults residing in $M_{23}C_6$. The M_7C_3/$M_{23}C_6$ and $M_{23}C_6$/M_6C boundaries, unlike that of cementite/M_7C_3, are curved, which may correspond to their weaker crystallographic relationships. From the observations mentioned above [11], since the $M_7C_3 \rightarrow M_{23}C_6$ transformation is the only one that would occur with evenly distributed shell carbide surrounding core carbide, the core (M_7C_3)-shell ($M_{23}C_6$) configured carbides could be formed. Previous studies have shown discovered core-shell structured carbides [28, 47, 48] and their effect on mechanical properties and performance in wear tests of HCCIs.

Tang et al. conducted studies on 45-series HCCIs, which contain 45wt% chromium and various carbon contents from 0 to 6wt% [7]. Only the 45-4 HCCIs showed a microstructure with core-shell structured carbides, as illustrated in Fig.4. With AES and EBSD analysis, the core carbides were determined to be M_7C_3 while the shell carbides and the eutectic carbides were $M_{23}C_6$.
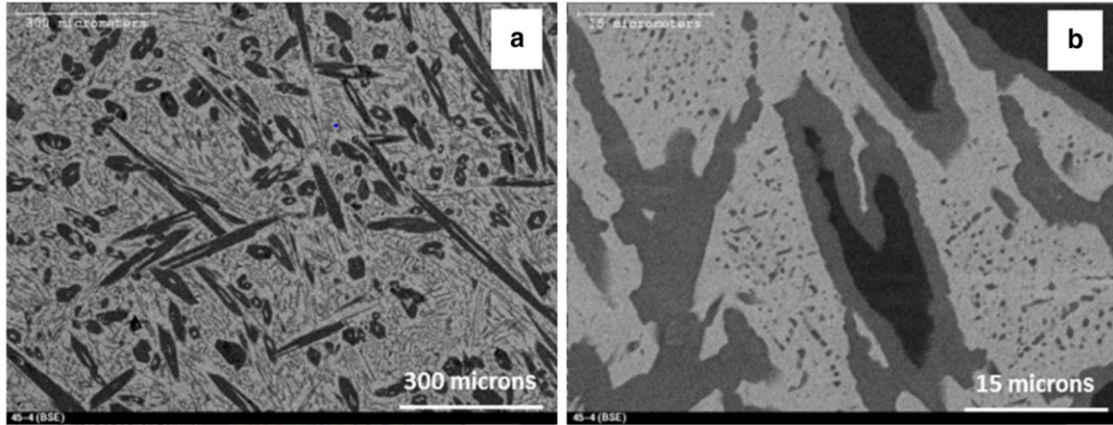
Fig.4 *SEM images with (a) low magnification and (b) high magnification [7].*

The mechanical and tribological properties of the 45-series HCCIs were obtained by bulk hardness tests, G65 abrasion and slurry-pot erosion tests. Results showed that the Fe-45wt%Cr-4wt%C HCCI exhibited the highest resistance to abrasion and erosion and the highest hardness as shown in Fig.5 and Fig.6, respectively. It was demonstrated that the excellent mechanical performance of 45-4 HCCI was attributed to its core-shell structured carbides. Hardness and Young's modulus of the core carbide (M_7C_3), shell carbide ($M_{23}C_6$) and matrix were investigated by a nano-indenter coupled with AFM. The hardness and Young's modulus decreased in the sequence of M_7C_3, $M_{23}C_6$ and matrix, presenting the mechanical mismatch between primary M_7C_3 carbides and ferrous matrix, which may introduce interfacial stress and cause failure during wear tests. The interfacial stress distribution was then analyzed by finite element method with various shell thicknesses. With the relatively softer shell layer($M_{23}C_6$), the maximum tensile stress between the ferrous matrix and primary carbides decreased extensively. Hence, the core-shell structured carbides were considered beneficial to the mechanical properties and wear resistance of HCCIs.
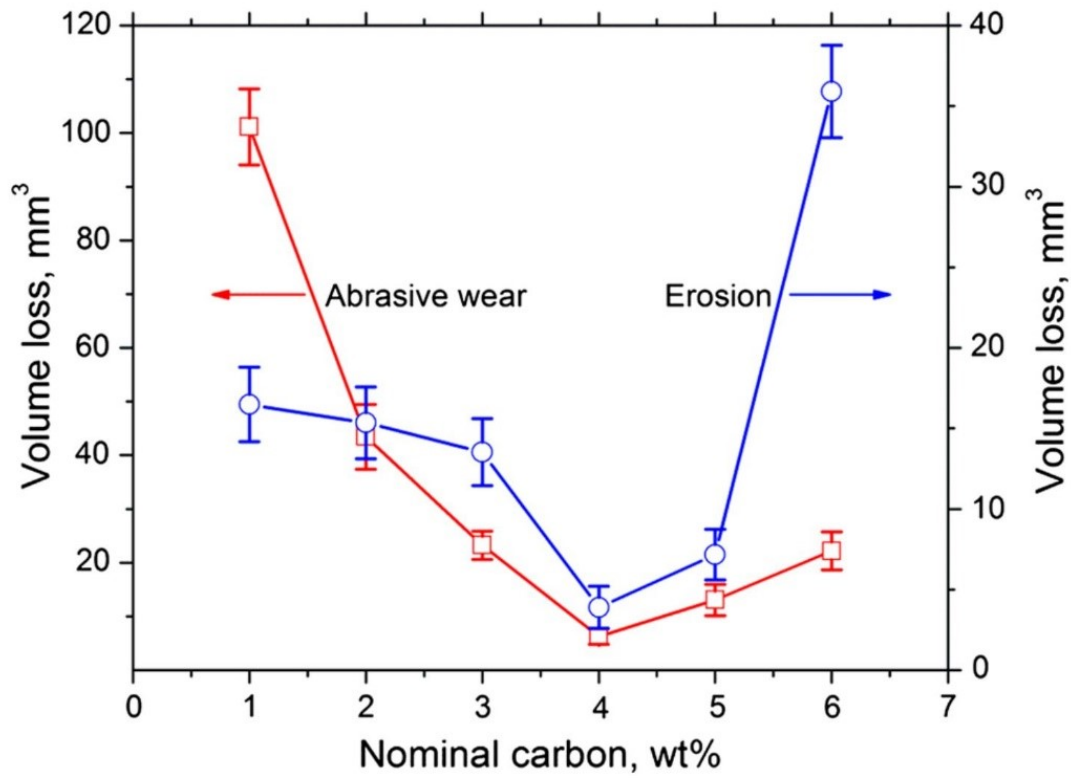
Fig.5 *Resistance of 45-series HCCIs to abrasive wear (red line) and slurry-pot erosion*

(blue line) [7].
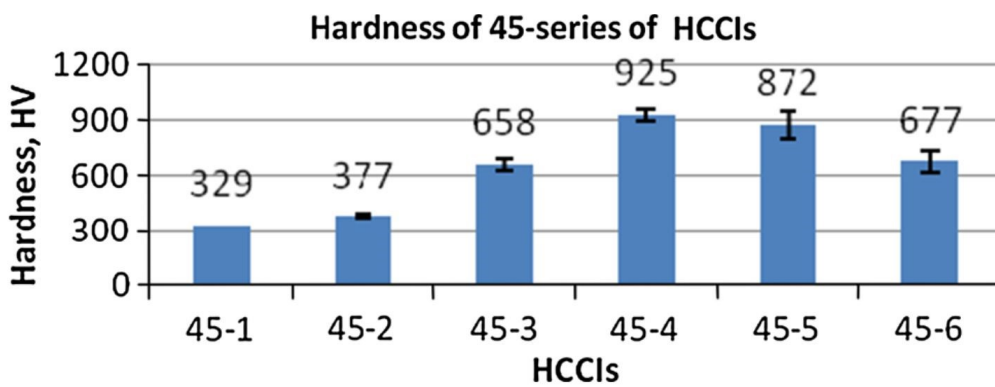
Fig.6 *Bulk hardness of 45-series HCCIs [7].*

In order to better understand the effect of core-shell structured carbides on tribological performance of HCCIs, studies [12] have been conducted by employing the micro-scale dynamic method (MSDM) on erosion simulation and finite element method (FEM) on stress/strain analysis. With addition of the medium hard phase, local interfacial cracking is reduced to the least possibility when the shell thickness is 8 μm according to MSDM simulation results. When the shell thickness continuously increases, the bulk hardness of materials decreases, leading to lower erosion resistance. According to the FEM analysis, a 4 μm-thickness shell carbide added between the matrix/M_7C_3 interface can decrease the principle stress by 61.9% and the shear stress by 31.5%. For vertically aligned carbides, the stress and strain decrease with increasing shell thickness. While for horizontally aligned carbides, the principle and shear stress first decrease with increasing shell thickness and reach a minimum at 6 μm, then slightly increase until saturation. If the thickness of the $M_{23}C_6$ shell is sufficiently large, the bulk hardness decreases and limits the carbides performance as reinforcing phases.

Since the beneficial effects of the core-shell structured carbides were confirmed, efforts were made to determine the processing condition to obtain such configured carbides. Wang and Li [13] utilized a thermo-kinetic analysis to investigate the mechanism, and most importantly, determined the compositional ranges for the formation of core-shell structured carbides. Equilibrium phase diagrams with various Cr contents from 10 to 45 wt% were calculated using thermodynamics database and the CALPHAD method to obtain the stable regions with phases consisting of M_7C_3, $M_{23}C_6$ and matrix, which is the basic phase assemblage of HCCIs with core-shell structured carbides. With fixed Cr content, the M_7C_3+ $M_{23}C_6$+matrix region would be stable with carbon content

between 0.06 wt% (Cr) to 0.1 wt% (Cr). The 3D phase diagram and the enlarged diagram for ternary M_7C_3 + $M_{23}C_6$ + matrix region are depicted in Fig.7. Any HCCI which has a composition within the blue area shown in Fig.7b may form the core-shell structured carbides.
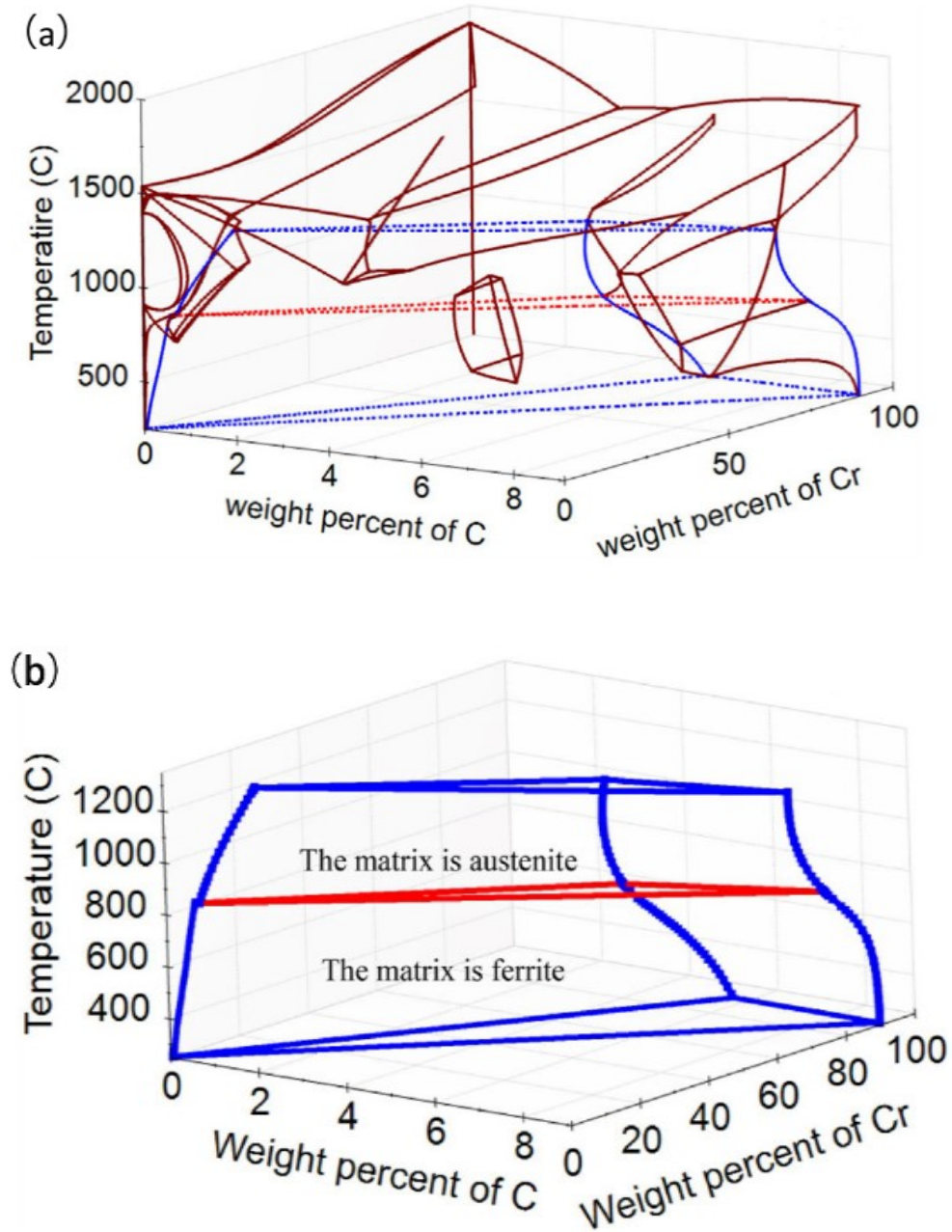
Fig.7 (a) 3D diagram and (b) the enlarged ternary $M_7C_3+M_{23}C_6$+matrix region [13].

The solidification process of nine alloys were then analyzed using Scheil-Gulliver and Lever-Rule methods to predict the solidification sequence and the as-cast microstructure. The former method deals with the situation close to rapid cooling, while the latter is suitable for extremely slow cooling processes. The realistic solidification process proceeds between the situations handled by the two methods but closer to the former one. According to the simulation, the most attractive as-cast microstructure is the M_7C_3+matrix eutectic colony, which may form core-shell structured carbides if $M_{23}C_6$ nucleates at the M_7C_3/matrix interface after post heat-treatment.

Even though the phase diagram indicates $M_{23}C_6$ is a stable phase, whether $M_{23}C_6$ would nucleate in the matrix or at the M_7C_3/matrix interface is dependent on the nominal composition, solidification process, as well as the post heat-treatment. The nucleation driving force of $M_{23}C_6$ at the M_7C_3/matrix interface has been calculated. In comparison to experimental results, for those alloys with observation of core-shell structured carbides, the calculated driving force exceeds 300 J/mol. Calculation results also reveal that higher heat treatment temperature would lead to lower driving force for $M_{23}C_6$ nucleating at the interface and austenite matrix would enlarge the driving force for nucleation of a $M_{23}C_6$ shell.

1.2.2.2 Refining primary carbides via alloying elements

Hypereutectic HCCIs usually exhibit improved abrasion resistance than hypoeutectic and eutectic HCCIs due to their higher volume fraction of carbides and thus higher overall hardness [49]. However, the higher hardness is achieved at the expense of fracture toughness caused by bulky primary M_7C_3.

One promising way to keep the toughness while increasing hardness is to decrease the size of carbides [50]. Previous studies showed some methods to achieve this goal such as rapid cooling [51, 52], lower superheat [53], fluctuation treatment [54] and alloying [55-57], in which rapid cooling and alloying were frequently discussed. Although finer microstructure may form as a result of rapid cooling, the influenced area is so limited that the feasibility of this method for commercial usage is quite low [9]. Compared to rapid cooling, alloying is more popular in industrial manufacturing. Studies have been conducted to investigate the effects of various alloying elements on improvement of microstructure, especially on the configuration of carbides in HCCIs. Elements such as Mg, B and Ti can segregate at the carbide/matrix interfaces and refine the eutectic carbides [57-59]. With the purpose of refining the primary carbides, strong carbide-forming elements like Nb, Ti and V were added in hypereutectic HCCIs and resulted in apparent improvement on wear resistance [60-62].

The afore-mentioned phenomenon has drawn great interest from researchers. It has been observed that the refined carbides usually have inoculant for heterogeneous nucleation [9, 50, 63-65]. The premise of the heterogeneous nucleation is described as follows [50, 65]:

1) Added alloying elements may form phases that have higher melting points than M_7C_3 carbide, which may act as the inoculant for heterogeneous nucleation of M_7C_3 carbides.

2) The interfacial energy of the inoculant/M_7C_3 interface is smaller than the solid-liquid interfacial energy of M_7C_3.

17

3) To achieve low interfacial energy (inoculant/M_7C_3), the lattice misfit between M_7C_3 and inoculant should be small enough. A parameter δ [66] describes the lattice mismatch:

$$\delta = \frac{a_C - a_N}{a_C} \tag{1.1}$$

where, a_C represents the atomic spacing of low index face of M_7C_3 carbides, whereas a_N represents that of the inoculant. Bramfitt [67] have proposed a theory that when $\delta < 6\%$, the heterogenous nucleation would be highly effective, while for $6\% < \delta < 12\%$, the nucleation would be moderately effective. As δ value increased to 12%, the nucleation would be ineffective.

For instance, Nb is a strong carbide-forming element and is widely used in steels and cast irons, which does not only form hard phases but also modifies the matrix. Recent studies [64, 65] have shown that NbC precipitates in Nb-alloyed materials first and acts as the inoculant for M_7C_3 heterogeneous nucleation, thus decreasing the size of M_7C_3 and refining the microstructure as shown in Fig.8. According to the thermodynamics analysis, NbC solidifies first. The solid-liquid interfacial energy of M_7C_3 was calculated using molecular dynamics, which was 3.312 J/m^2. The interfacial energy of NbC/M_7C_3 was calculated using the first-principles method, which ranged between 2.8-4.6 J/m^2. Hence, there is a region that the NbC/M_7C_3 interfacial energy could be lower than the solid-liquid interfacial energy of M_7C_3.
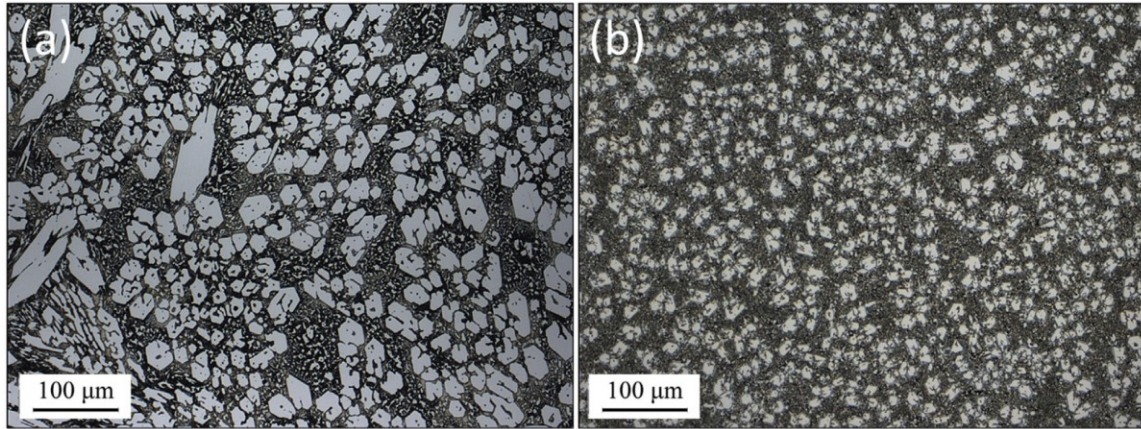
Fig.8 *Microstructure of hypereutectic Fe-Cr-C alloys with (a) 0 Nb and (b)1.2wt%*

Nb [64].

The same situation appears when Ti is added. Ti is also a strong carbide-forming element. TiC was shown to be the inoculant for heterogeneous nucleation of carbides and austenite [57, 68-70]. The formation temperature of TiC is 3338K [71], while the melting point of M_7C_3 was calculated to be 1625±5K [64]. Thus, TiC precipitates first during solidification of HCCIs. The lattice parameter of TiC and M_7C_3 was calculated using the first-principles method [8, 72]. The misfit between both phases is small enough for nucleation.

Ce also shows its capability to refine M_7C_3 but the mechanism for its refining effect is slightly different. Ce does not react with carbon. Instead, it reacts with the impurity elements such as S and O to form Ce_2S_3 and Ce_2O_2S [50, 73]. This deoxidation and desulfuration effect of cerium purifies the material and provides the inoculants for M_7C_3 carbides to decrease the size of the hard phase, contributing to improved impact toughness of HCCIs with cerium addition.

1.2.2.3 Doping alloying elements in carbides

Despite forming core-shell structured carbides and refining the primary M_7C_3 carbides, doping alloying elements in M_7C_3 is also an effective way to improve the mechanical properties of HCCIs. By dissolving alloying elements in M_7C_3, its mechanical properties can be modified such that the elastic modulus and hardness of the carbide increase.

As a complex carbide, the simplest situation of M_7C_3 precipitated in HCCIs is the ternary $(Fe, Cr)_7C_3$ [6, 74]. When the Cr/Fe ratio in $(Fe, Cr)_7C_3$ varies as Cr concentration in HCCIs changes, its properties have been studied by experiments and first-principles calculations. Zhang et al. [74] have stated that among all $Fe_{7-x}Cr_xC_3$ carbides, the $Fe_3Cr_4C_3$ is the most stable one and has the largest elastic modulus and hardness. It is in accordance with the calculated and experimental results in studies of Cui et al. [6].

In order to determine the influence of other alloying elements on the properties of M_7C_3, strong carbide forming elements, such as W and Mo, were doped in the carbides [24]. From EDS data, W and Mo concentrations in primary M_7C_3 increase linearly with increasing amounts of W and Mo in the specimens. It is also noticed that W and Mo atoms preferentially substitute Fe instead of Cr in M_7C_3. The fracture toughness of the M_7C_3 carbide is measured by the indentation fracture method as depicted in Fig.9 and calculated by the following equation:

$$K_c = \alpha(EP)^{\frac{1}{2}}\left(\frac{d}{2}\right)a^{-\frac{3}{2}} \tag{1.2}$$

where, K_c is the fracture toughness, α is a calibration factor, E is Young's modulus and P is the indentation load.

The measured fracture toughness of W-doped or Mo-doped M_7C_3 is similar regardless of the W and Mo concentration. However, hardness of the carbide slightly elevates with doped W or Mo at room temperature. As temperature increases, hardness decreases. But Mo and W more or less suppress the decrease in the carbide's hardness as temperature increases, indicating that they can also maintain the high temperature hardness of M_7C_3.
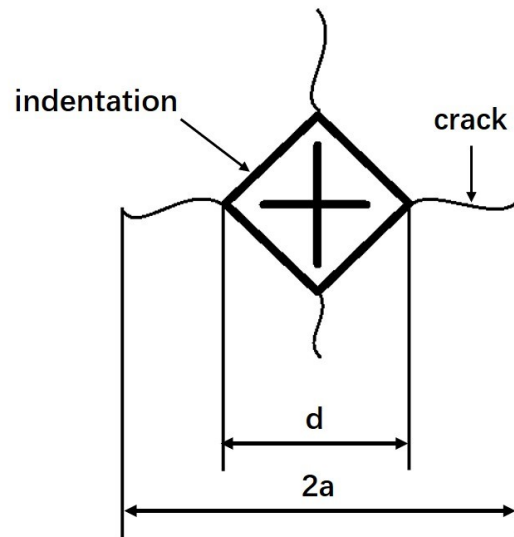
Fig.9 Indentation fracture method

To analyze a more complicated situation, a computational method has been utilized to build ternary, quaternary and penternary M_7C_3. Chong et al. [23] have used $Fe_3Cr_4C_3$ as the initial carbide, doping with W, Mo and/or B, to analyze the mechanical properties of $Cr_3Fe_3WC_3$, $Cr_3Fe_3MoC_3$, $Cr_3Fe_3W_{0.5}Mo_{0.5}C_3$, $Cr_4Fe_3C_2B$, $Cr_3Fe_3WC_2B$,

$Cr_3Fe_3MoC_2B$ and $Cr_3Fe_3W_{0.5}Mo_{0.5}C_2B$. Elastic matrices can be obtained by first-principles calculations and used for calculation of mechanical properties, such as bulk modulus B_v, shear modulus G_v and Young's modulus E. Young's modulus and Pugh's ratio, B_v/G_v, can be used to evaluate the strength and toughness of M_7C_3, respectively. Hardness can also be calculated via equation using bulk modulus and shear modulus. The study has shown two methods of balancing the ductility and strength of M_7C_3 carbide. One is to increase the ductility but not significantly decrease the moduli of M_7C_3 carbide by doping W + B or W + Mo, while the other is to enhance the hardness with a small decrease in toughness by doping Mo + B or W + Mo + B. Both methods mentioned above can be considered effective ways to improve the wear resistance of HCCIs.

Chapter 2 Methodology

2.1 CALPHAD

In this study, a thermodynamics technique, CALPHAD method, is applied to calculate phase diagrams and properties of alloys including Gibbs energy of each phase and volume fraction of phases, etc. The CALPHAD approach is described in this section. The basic thermodynamics knowledge that underpinned CALPHAD as well as its computational methods are also introduced.

2.1.1 Basic thermodynamics

Systems, whether they are in solid, liquid or gaseous state, are called solutions when there is solubility between their components [75]. The solution model is vital since the CALPHAD method, in many cases, is applied to such systems. Systems rarely only involve pure stoichiometric compounds. The simplest case, binary solution is first discussed and relevant formulas that are applied to more general situations are shown in this section.

2.1.1.1 Gibbs energy of binary solutions

The general formula of Gibbs energy of a solution [76] is defined as:

$$G = G^o + G_{mix}^{ideal} + G_{mix}^{xs} \tag{2.1}$$

where, G^o is the Gibbs energy of the pure components, G_{mix}^{ideal} is contributed to the ideal mixing process, G_{mix}^{xs} is related to the non-ideal interactions between components.

In an ideal binary solution, the molar Gibbs free energy of mixing can be given by [75]:

$$G_{mix}^{ideal} = RT(x_A ln x_A + x_B ln x_B) \qquad (2.2)$$

where the x_A and x_B are the mole fraction of A and B atoms, respectively.

The excess Gibbs energy is described as:

$$G_{mix}^{xs} = x_A \bullet x_B \bullet \Omega \qquad (2.3)$$

where Ω is the interaction energy parameter for regular solutions. If a solution exhibits a positive deviation from ideal mixing, Ω has a positive value; and if the solution shows a negative deviation from ideal mixing, Ω has a negative value. A positive value of Ω would lead to a 'hump' of the G curve, as shown in Fig.10 [75]. The alloys, which have compositions between x_1 and x_2 can lower their Gibbs energy by forming two phases, A-rich phase with composition x_1 and B-rich phase with composition x_2. Thus, miscibility gaps would show on phase diagrams.
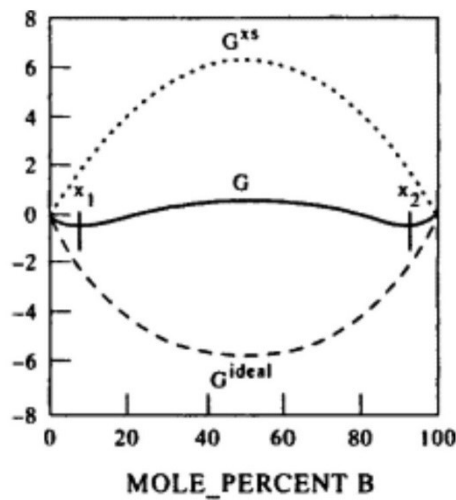
Fig.10 *Gibbs energy of A-B system showing repulsive interactions [75].*

2.1.1.2 Partial Gibbs energy of binary solutions

Another fundamental concept, partial Gibbs energy of mixing, has then arisen. The relationship of partial Gibbs energy $\bar{G}_A$, $\bar{G}_B$ and integral Gibbs energy of mixing in A-B system can be given by [75]:

$$G_{mix} = G_{mix}^{ideal} + G_{mix}^{xs} = x_A\bar{G}_A + x_B\bar{G}_B \qquad (2.4)$$

The partial Gibbs energy is related to the activity of components in solution. Activity a_i of component i can be defined as:

$$a_i = \frac{p_i}{p_i^o} \qquad (2.5)$$

where p_i is the measured vapor pressure of i and p_i^o is the standard vapor pressure of component i.

In an ideal solution, activity of component i is equal to the mole fraction of i. With a negative interaction (Ω<0), the activity has a negative deviation from the ideality, while in the case of positive interactions (Ω>0), positive deviation of activity is shown.

The relationships of partial Gibbs energy of mixing, partial excess energy of mixing and activity are given by:

$$\bar{G}_i = RTln(a_i) \qquad (2.6)$$

$$\bar{G}_i^{xs} = \bar{G}_i - \bar{G}_{ideal} = RTln(a_i) - RTln(x_i) = RTln\left(\frac{a_i}{x_i}\right) \qquad (2.7)$$

2.1.1.3 Gibbs energy of multi-component solutions

In a multi-component system, the G^o term and G_{mix}^{ideal} term can be calculated similarly as in the binary solution [75]:

$$G^o = \sum_i x_i \, G_i^o \tag{2.8}$$

$$G_{mix}^{ideal} = RT \sum_i x_i \, lnx_i \tag{2.9}$$

where x_i is the mole fraction of component i and G_i^o is the Gibbs energy of pure i.

However, the excess Gibbs energy is more complicated and involves non-regular terms which is based on the Redlich-Kister equation [75, 77]:

$$G_{mix}^{xs} = \sum_{i=1}^{n} \sum_{j=i+1}^{n+1} x_i \, x_j \left[\Omega_{ij}^0 + \Omega_{ij}^1 (x_i - x_j) + \Omega_{ij}^2 (x_i - x_j)^2 \, ... \right] \tag{2.10}$$

2.1.2 Computational methods

In the CALPHAD method, the main issue is to calculate equilibria by minimizing Gibbs energy. Computational methods are of importance during the minimization process and optimization codes are applied to reduce statistical errors. In this section, the method of calculating two-phase equilibria in binary systems, which is the simplest case, is demonstrated. The principles can then be applied to more complicated multi-component systems. Optimization codes are also discussed.

2.1.2.1 Two-phase equilibria in binary system

The total Gibbs energy of a system can be calculated either by partial Gibbs energy $\bar{G}_i$ of component i or Gibbs energy of each phase in the system [78]:

$$G = \sum_i n_i \bar{G}_i = \sum_\Phi N^\Phi G_m^\Phi \tag{2.11}$$

where n_i is the amount of component i, N^Φ is the amount of phase Φ and G_m^Φ is the molar Gibbs energy of phase Φ.

In the equilibria with two phases, the amount of each phase can be calculated using the lever rule:

$$N^{\Phi_1} = \frac{|x_i - x_i^{\Phi_2}|}{|x_i^{\Phi_1} - x_i^{\Phi_2}|} \tag{2.12}$$

$$N^{\Phi_2} = \frac{|x_i - x_i^{\Phi_1}|}{|x_i^{\Phi_2} - x_i^{\Phi_1}|} \tag{2.13}$$

where N^{Φ_1} and N^{Φ_2} are the amounts of phase Φ_1 and Φ_2, respectively, x_i is the composition of the alloy, and $x_i^{\Phi_1}$ and $x_i^{\Phi_2}$ are the composition of phases Φ_1 and Φ_2, respectively.

We may assume that the alloy composition and temperature of the system are known and there is only one phase (Φ_1) in the system at start point, a certain amount of phase Φ_2 is then added, which leads to a change in composition with varied amount of phase Φ_1 according to the above-mentioned equations. As The composition of phase Φ_1 is then kept constant, N^{Φ_2} and $x_i^{\Phi_2}$ are changed to find the minimized G. The G/N^{Φ_2}

curve can be drawn, and G is minimized when dG/dN^{Φ_2} equals zero. The preliminary value of N^{Φ_2} can be randomly guessed and the next guess can be made by calculating the second differential of G/N^{Φ_2} curve and utilizing the Newton-Rapson method. The next step is to keep constant composition of phase Φ_2 and change N^{Φ_1} until minimized G is achieved. The cycle is repeated until the difference of total Gibbs energy between latest two iterations satisfies the convergence limit. Hence, the composition and amount of both phases in equilibrium state are calculated.

The method demonstrated above is generally used. If an alloy is in single-phase equilibrium, this method can recognize and converge the alloy to the correct single-phase equilibrium. Moreover, in a system with numerous phases, it is capable to check their stability and find the true equilibrium state [79].

2.1.2.2 Calculation of multi-component systems

In a multi-component system, to calculate the Gibbs energy of the system, the degrees of freedom need to be reduced. Constraints, such as mass balance and composition range, are defined. White et al. [80] have mentioned that the Gibbs energy of a mixture can be calculated by defining the chemical potential of species i and constraining the mass balance:

$$\bar{G}_i = \bar{G}_i^o + RTlna_i \tag{2.14}$$

$$\sum_i a_{ij} x_i = n_j \quad (j = 1, 2, \dots, m) \tag{2.15}$$

where $\bar{G}_i^o$ is the standard chemical potential of species i, a_{ij} represents the number of element j in species i, x_i is the amount of species i and n_j is the total amount of element j in the system.

Two methods were presented to minimize Gibbs energy. Dantzig et al. [80] mentioned a linear programming method by using the following equation:

$$\frac{G}{RT} = \sum_i x_i \left[\left(\frac{\bar{G}_i^o}{RT} \right) + ln \frac{x_i}{x_{total}} \right] = \sum_i x_i \left(\frac{\bar{G}_i^o}{RT} \right) + x_{total} \sum_i \left(\frac{x_i}{x_{total}} \right) ln \left(\frac{x_i}{x_{total}} \right) \quad (2.16)$$

Thus, G can be expressed as a linear function of $(x_i/x_{total}) ln (x_i/x_{total})$ and then minimized.

Another method is called steepest descent, which is a rapid solution and thus used in software codes [81]. G(Y), as a function of composition, is defined first, and a set of composition guesses which is constrained by Eq. (2.16) is used in G(Y). The function is then expanded utilizing Taylor's approximation and minimized by using Lagrange multiplier [82] or the Newton-Raphson method [83]. The results of G(Y) can be estimated as the input of the next iteration. Convergence is reached when the Gibbs free energy difference is less than the criterion.

2.1.2.3 Optimization of phase diagrams

Optimization of calculated phase diagrams is usually required due to the existence of systematic errors caused by faulty calibration or inappropriate measurement techniques in experiments and is achieved by establishing optimization software.

One of the first programs is the Lukas program [84]. The initial code utilized the Gaussian least-squares method [84] while the later one also introduced the Marquardt method [85]. The program gives equation of errors from three aspects: calorimetric measurements, EMF and vapor pressure measurements, and phase diagram information. Despite the mathematical methods, personal judgement is also required in the programme, which may affect the optimization results.

The PARROT program [86], which is used in Thermo-Calc software, applies a criterion of best fit to reduce experimental and calculated data. The criterion can be expressed as follow:

$$L = \prod_{i=1}^{N} F_i \left(\bar{z}_i^o, \overline{w}_i \right) \tag{2.17}$$

where L is the likelihood function, N is the number of experimental observations, F_i is the multi-variable density function, $\bar{z}_i^o$ is the measured experimental value and $\overline{w}_i$ represents the statistical parameters in F_i.

When L is maximized, the model has best estimated parameters. The calculation of L requires the density function of all experiments, which is rarely obtained. Hence, an assumption of F_i is expressed with respect to the true value $\bar{\mu}_i$ of experimental data:

$$F_i = 2\pi - \frac{nz_i}{2} \left(\det V_i \right)^{1/2} \exp \left[-\frac{1}{2} (\bar{z}_i^o - \bar{\mu}_i)^T V_i^{-1} (\bar{z}_i^o - \bar{\mu}_i) \right] \tag{2.18}$$

where, V_i is the matrix of the measured variables.

Assuming the maximation of L coincides with minimum value of the exponential part in Eq. (2.18), the estimator S, which needs to be minimized, can be expressed as:

$$S = \sum_{i=1}^{N} [(\bar{z}_i^o - \bar{\mu}_i)^T V_i^{-1} (\bar{z}_i^o - \bar{\mu}_i)] \qquad (2.19)$$

S can be simplified by using a reasonable assumption that the off-diagonal elements of V_i are zero and represented by taking another set of data $\bar{u}_i^o$, which does not show serious inaccuracy, into account. S is then minimized by a finite difference approximation [87].

2.2 First-principles calculations

In this thesis, the *Ab initio* method is utilized to solve subatomic problems without considering external effects such as temperature and time. This method is based on quantum mechanics that involves complex equations. Thus, approximations were developed to simplify those equations. The method started with several atoms, until density functional theory (DFT) showed up and dealt with systems containing 10^2-10^3 atoms, by which one can obtain both electronic and magnetic properties.

2.2.1 Schrödinger equation and its approximation

The Schrödinger equation is a partial differential equation which shows the wavefunction of a quantum-mechanical system [88]. It can be expressed as [89]:

$$H\Psi\ (r, R, t) = E\Psi\ (r, R, t) \qquad (2.20)$$

where, the H is the Hamiltonian operator, Ψ represents the wavefunction, E is the energy, t is time, r and R are the electron and nucleus coordinates respectively.

Due to the complexity of the equation, efforts were made develop approximations and solve the equation [90, 91]:

1. Since ground state of a system is time-independent, we only deal with the ground state at 0K.

2. The gravity and relativity of electrons are ignored, due to its small mass and slower speed than light.

3. Since nuclei are more massive than electrons, electrons move much faster than nuclei and their motion can be treated separately. In the Born-Oppenheimer approximation, the total energy is considered as the sum of independent terms: $E_{total} = E_{electron} + E_{nucleus}$.

According to the above approximations, the Schrödinger equation can be expressed as:

$$H\Psi(r) = E\Psi(r) \tag{2.21}$$

2.2.2 Density functional theory

With approximations mentioned above, one may solve problems in simple systems. However, the density functional theory proposed in the 1960s made it possible to deal with complex systems.

2.2.2.1 Hohenberg-Kohn theorem

Two theorems were brought out by Hohenberg and Kohn [92] in order to relate electron density, $n(r)$, to energy, wave function and Hamiltonian. The electron density only has three variables, so that the Schrödinger equation is much simpler, and the feasibility of calculation is largely improved.

The first theorem states that the electron density completely determines all properties of a system:

$$E[n(r)] = E_{v(r)}[n(r)] + F[n(r)] \qquad (2.22)$$

Here, $v(r)$ is the external potential, $F[n(r)]$ is a function related to system-independent internal potentials.

The second theorem is that with specific $v(r)$, the $E_{v(r)}[n(r)]$ can be minimized, and the ground state can thus be found.

2.2.2.2 Kohn-Sham equation

Since the calculation of energy of a large system based on electron density is difficult, a fictitious system was constructed by Kohn and Sham [93] that electrons were considered non-interacting and were in an effective potential, v_{eff}, which generated the same electron density as in interacting system.

The effective potential includes not only the external potential $v(r)$, but also an exchange-correlation potential, $v_{xc}(r)$, which is defined as:

$$v_{xc}(r) = \frac{\delta E_{xc}[n(r)]}{\delta n(r)} \qquad (2.23)$$

The exchange-correlation energy can thus be calculated accordingly. However, the $v_{xc}(r)$ is an unknown term, which needs further approximation. Two approximations, local density approximation (LDA) and generalized gradient approximation (GGA) are most used nowadays. LDA can achieve a realistic description of atomic structure, elastic and vibrational properties but is not accurate to describe energies of chemical reactions,

which results in overestimation of the binding energies [94, 95]. GGA was thus developed to overcome the deficiencies of LDA and is extensively used due to its higher accuracy.

2.3 Atomic force microscopy

The atomic force microscope (AFM) is a part of a large family called the scanning probe microscopes (SPMs) [96]. It is a powerful non-destructive characterization technique which can be used in vacuum, air and fluid [97-100]. The AFM is capable to obtain high-resolution topographic images, as well as chemical, mechanical, electrical and magnetic properties [97, 101]. Thus, it is widely used in materials engineering and its allied fields.

2.3.1 Basic AFM components

A basic set-up of AFM is illustrated in Fig.11 [96]. The cantilever has a tip (probe) at its free end to interact with the tested surface. Commercially manufactured cantilevers and tips are normally Si_3N_4 or Si and the upper surface of cantilevers are coated with a reflective gold or aluminum layer, so that the laser beam can be reflected to the photodetector. The attractive or repulsive force between tip and surface would deflect the cantilever; thus the reflection path of the laser beam is changed, producing a change in the position of a spot on the photodetector.
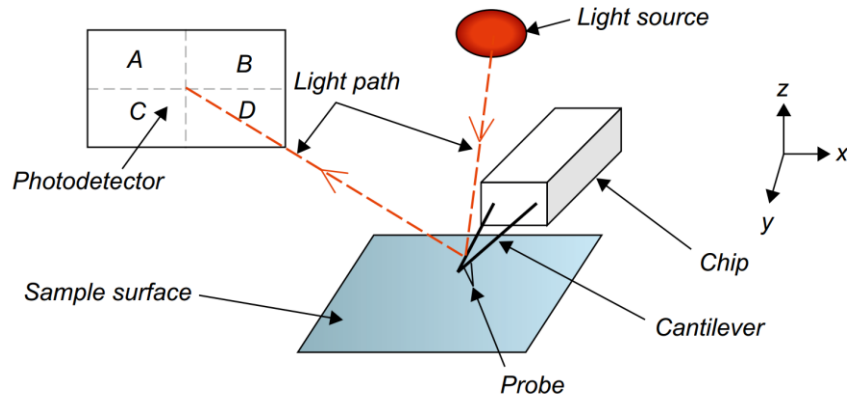
Fig. 11 *Schematic presentation of atomic force microscope [96].*

2.3.2 Imaging modes

There are three typical imaging modes available in AFM, the contact mode, the non-contact mode and the tapping mode [102]. The interaction forces between tip and surface in theses modes are different. As the tip and surface separated largely, no interaction exists. When the distance decreases, attractive van der Waals force pulls the tip towards the surface. However, as contacts are made, repulsive forces would repel the tip away from the surface.

In contact mode, the distance between tip and surface is less than 0.5 nm; therefore, repulsive van der Waals interaction happens [102]. This mode is the simplest mode and suitable for hard and flat surfaces, so that the high contact force can less damage the sample or probe. Two drawbacks are observed in this mode. One is that the lateral force when pass steep edges or the adhesive and frictional forces during scanning can damage the probe and sample. The other is that the deformation of sample surface leads to inaccurate height and larger contact area, both of which result in lower resolution.

In order to overcome the disadvantages of the contact mode, the tapping mode was developed [103-105]. In this mode, the cantilever vibrates at a frequency slightly smaller than the resonant frequency and an amplitude that ranges from 20 to 100 nm. It is suitable to test soft materials and films since the probe only contacts the surface for a short duration and the lateral force is largely decreased. However, the impact force as the tip strikes the surface during oscillation may be higher than that in the contact mode.

In the non-contact mode, the cantilever still oscillates but at a frequency higher than the resonant frequency and a much smaller amplitude [96, 102]. The distance between the probe and surface is kept between 0.1-10 nm. This mode is more versatile than the tapping mode. For instance, for scanning fluid, the liquid layer may be too thick so that the probe may either be out of the van der Waals force range or trapped by the fluid layer. In this case, the non-contact mode would work better.

Chapter 3 Promoting the formation of core-shell structured carbides in high-Cr cast irons by boron addition

3.1 Experimental and calculation methods

3.1.1 Materials preparation

In this study, base alloys are high-Cr cast irons containing 45wt% chromium, 3wt% and 5wt% carbon, respectively, balanced by iron. No core-shell structured carbide was found in the base alloys in previous studies. B additions of 1.1 wt% and 0.8 wt% boron were added to Fe-45wt%Cr-3wt%C alloy and Fe-45wt%Cr-5wt%C, respectively, to determine if the B additions favor the formation of core-shell structured carbides in the alloys. Four sample alloys denoted as Fe45Cr3C, Fe45Cr5C, Fe45Cr3C1.1B and Fe45Cr5C0.8B, respectively, were made using an arc furnace. The alloy melt was poured into a copper mold in a high purity argon atmosphere and cooled down by compressed air. Samples were cut from the ingots. In order to compare the as-cast microstructures with that experienced annealing as well as those predicted from thermodynamics calculations, samples FeCr3C and Fe45Cr3C1.1B were annealed at 650°C for 4 hours, while samples Fe45Cr5C and Fe45Cr5C0.8B were annealed at 900°C for 4 hours, followed by cooling in water. Annealing temperatures were chosen based on calculated phase diagrams (Fig.12b and Fig.12c) to reach the phase regions where M_7C_3 and $M_{23}C_6$ coexist so that the core-shell structured carbides may form. Samples with the same carbon concentration were heat-treated at the same temperature to rule out the possibility that the formation of core-shell structured carbides were induced by the annealing process.

3.1.2 Characterization and mechanical testing

The surface of specimens was ground using SiC papers and polished with alumina powder. Microstructural observation was carried out using SEM (Tescan Vega-3) in backscattered electron mode, and compositions of individual phases were measured by equipped EDS (Energy Dispersive Spectroscopy). Phase analysis was carried out using an X-ray diffractometer (Rigaku Ultima IV) with Co Kα radiation. The scan range was set from 30° to 90° 2θ at a scan speed of 2°/min. Auger Microscope (JEOL, JAMP-9500F) was employed to analyze the element distribution.

3.1.3 Calculation method

ThermoCalc [106] software with database TCFE6 was used to calculate equilibrium phase diagrams, volume fractions of various phases and the driving force for $M_7C_3{\rightarrow}M_{23}C_6$ transformation. The calculated phase diagrams were used to predict the compositional range of boron for forming core-shell structured carbides in both the Fe45Cr3C and FeCr5C alloys.

First-principles calculations were conducted with the density functional theory (DFT) as implemented in the Vienna ab initio simulation package (VASP) [107, 108]. The exchange-correlation energy was calculated within the generalized gradient approximation (GGA) of Perdew-Burke-Ernzerhof (PBE) [109]. A cutoff energy for plane-wave basis was set to be 450 eV for relaxation of bulk materials, surfaces and interfaces. The equilibrium states were achieved when electronic convergence reached 10^{-4} eV. While for elastic constants calculation, a 600 eV plane-wave cutoff energy was adopted. A k-point grid of $7{\times}7{\times}7$ was utilized for bulk $M_{23}C_6$ and $M_{23}(C, B)_6$ and that for

bulk M_7C_3 was 7×7×9. The k-point sampling for BCC Fe was 11×11×11. For each surfaces and interfaces, a 15Å vacuum layer has been added. A k-point sampling of 7×7×1 was adopted for $M_{23}C_6$, $M_{23}(C, B)_6$, M_7C_3 and Fe slabs, as well as all interfaces.

3.2 Results and discussion

3.2.1 Thermodynamic analysis

Equilibrium phase diagrams were calculated using the CALPHAD method for Fe45Cr3C, Fe45Cr5C, Fe45Cr3CB and Fe45Cr5CB alloy. The quasi-binary diagrams are depicted in Fig.12. According to the phase diagrams shown in Fig.12a, the three-phase region of M_7C_3+$M_{23}C_6$+α-Fe, in which CSSCs may form, does not appear in Fe45Cr5C, but exists in the Fe45Cr3C alloy when the temperature is below 372.2℃. However, below 372.2℃ there is no sufficient thermal energy or driving force for $M_{23}C_6$ to develop in the HCCI. The thermodynamic analysis is consistent with previous studies [7], in which no core-shell structured carbides were observed in Fe45Cr3C and Fe45Cr5Calloys.

The situation changes when boron is added to Fe45Cr3C alloy (Fig.12b), a α-Fe+M_7C_3+$M_{23}C_6$+ Cr_2B region shows up and keeps stabilized up to higher temperatures as boron content increases. To verify the thermodynamic analysis and determine if CSSC can be produced by alloying B, we added 1.1wt% boron to Fe45Cr3C alloy (see section 3.2.2 for details). As shown Fig.12b, along with a dashed line one may see that M_7C_3 and $M_{23}C_6$ co-exist at temperatures up to nearly 700℃, providing more thermal energy for CSSCs to develop in annealed HCCI castings. For the Fe45Cr5C alloy, according to Fig.12c, $M_{23}C_6$ is destabilized as temperature decreases and vanishes when the temperature is below ~800℃. Thus, the formation of CSSCs requires heat treatment or

annealing at a temperature between 800-1200°C. In order to obtain phase constituents of γ-Fe+ M_7C_3+$M_{23}C_6$, 0.8wt% of boron was added (see dashed line in Fig.12c) and the alloy was then annealed at 900°C, followed by water cooling. Details of the experimental study are given in section 3.2.2.

(a)
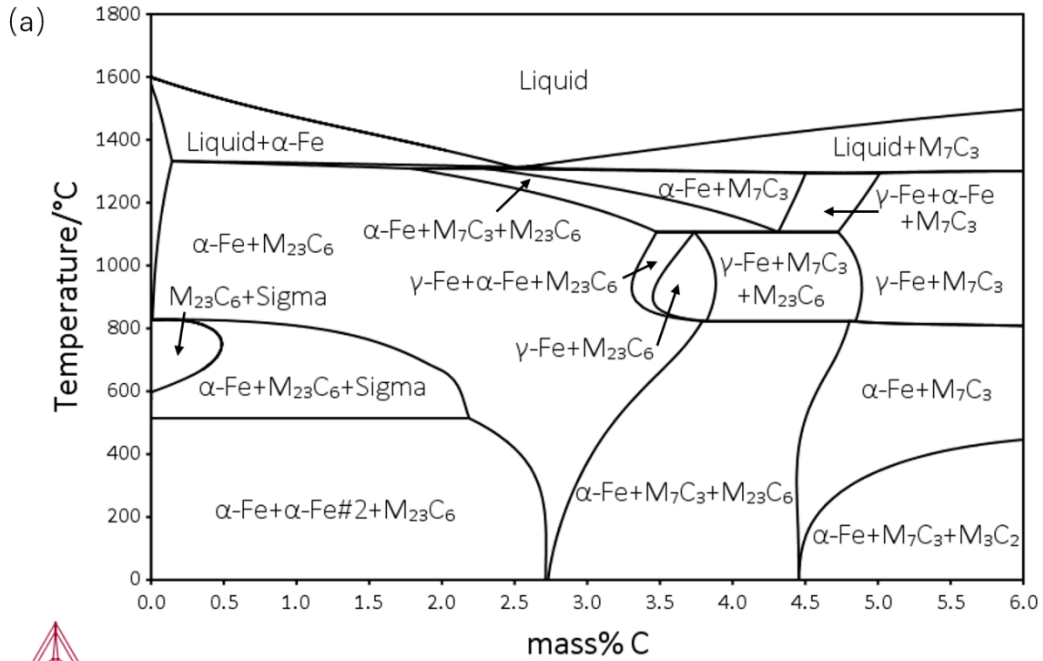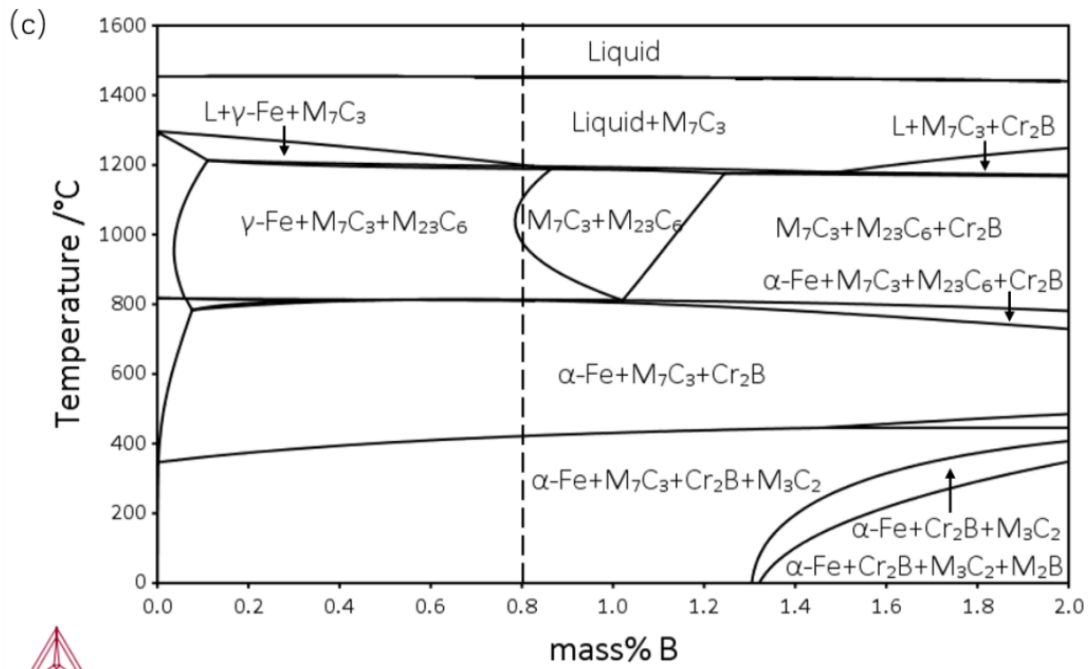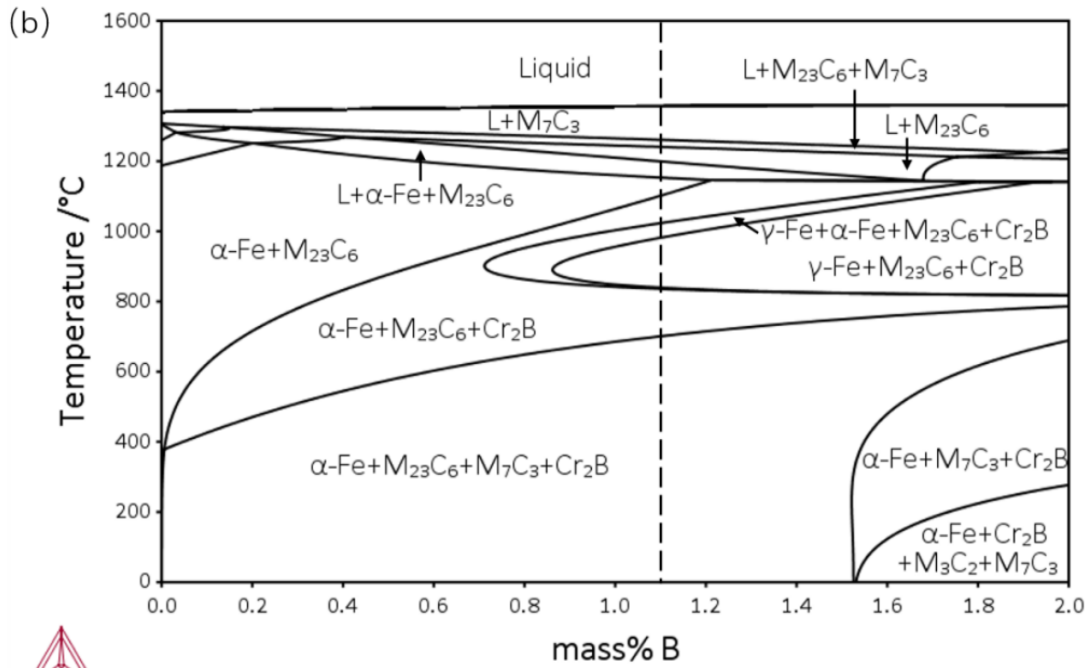
Fig.12 *Quasi-binary diagrams for (a) FeCr alloy, (b) FeCr3CB alloy and (c)*

FeCr5CB alloy.

Volume fractions of phases in Fe45Cr3C1.1B alloy and Fe45Cr5C0.8B alloy versus temperature were also calculated and are shown in Fig.13. According to Fig.12b and Fig.13a, in equilibrium status, solidification of primary M_7C_3 is followed by a $M_7C_3 \rightarrow M_{23}C_6$ transformation and Cr_2B precipitates subsequently. At 702.2°C, the volume fraction of M_7C_3 phase and that of α-Fe phase increase simultaneously, accompanied with a decrease in volume fraction of $M_{23}C_6$ phase. This phenomenon indicates that $M_{23}C_6$ becomes less stable as temperature decreases.

In Fe45Cr5C0.8B alloy (Fig.12c and Fig.13b), Cr-rich primary M_7C_3 carbide forms firstly. As temperature decreases to ~1200°C, the amount of M_7C_3 and liquid phase are reduced, resulting in the formation of Fe-rich $M_{23}(C, B)_6$. When temperature decreases to 812.1°C, the reaction $M_{23}(C, B)_6 \rightarrow M_7C_3 + α\text{-Fe} + Cr_2B$ happens which results in complete dissolution of $M_{23}(C, B)_6$. This process is accompanied with a γ-Fe→α-Fe transformation. From the solidification path of both B-added alloys, Fe45Cr5C0.8B alloy is considered to possess a higher probability to form core-shell structured carbides in the temperature range of 812 ~ 1200°C. During fast cooling, the γ-Fe+ M_7C_3 colony forms first, in which $M_{23}C_6$ can easily nucleate at the matrix/M_7C_3 interface during annealing. As for the FeCr3C1.1B alloy, the primary carbide is $M_{23}C_6$ when in equilibrium state. It would be easier for M_7C_3 to nucleate inside the matrix than being the inner core of carbides.
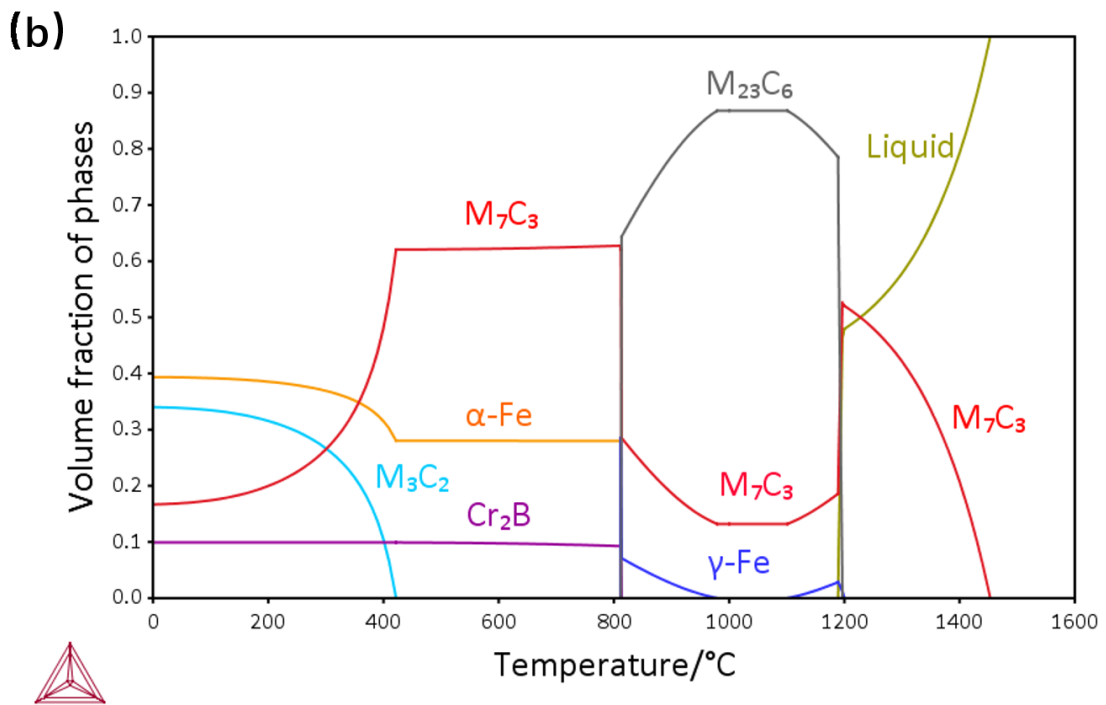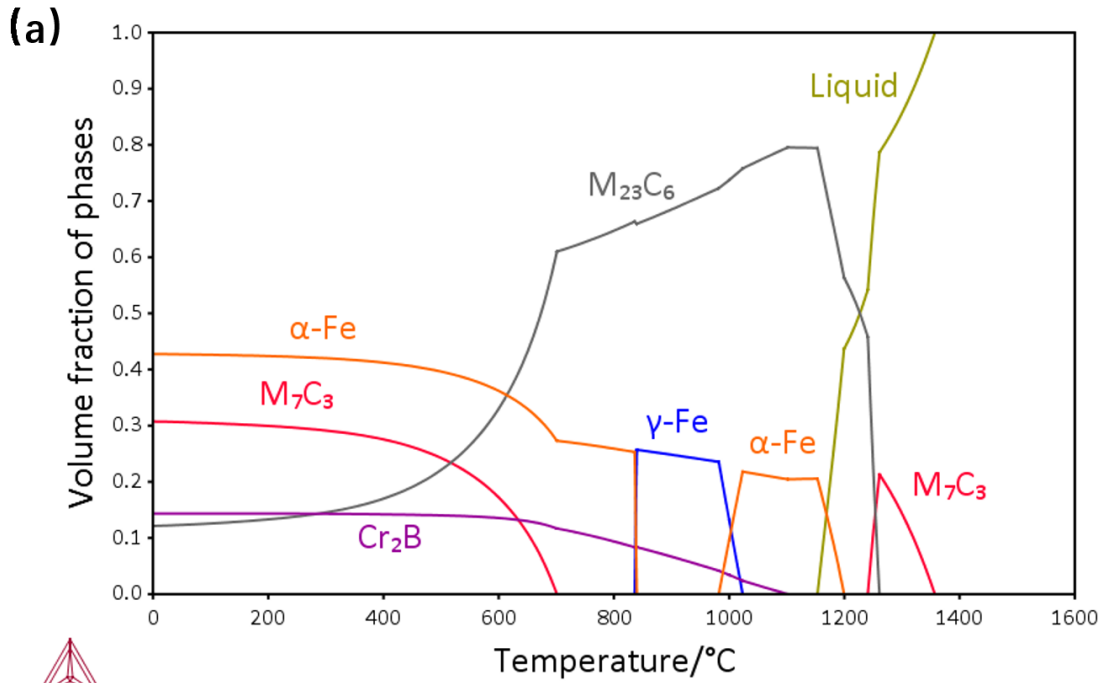
Fig.13 *Calculated volume fractions of phases versus of temperature of (a) Fe45Cr3C1.1B and (b) Fe45Cr5C0.8B alloy in equilibrium state.*

To demonstrate the role of boron in promoting the formation of core-shell structured carbides, Gibbs energies of M_7C_3 and $M_{23}C_6$ in Fe45Cr5C0.8B alloy at 900°C were calculated and are shown in Fig.14. Coinciding with Fig.12c, no $M_{23}C_6$ exists in B-free Fe45Cr5C alloy. As the amount of boron increases, the Gibbs energy of M_7C_3 initially increases until reaching the maximum where the boron content is about 0.85wt%, then decreases. However, the Gibbs energy of $M_{23}C_6$ changes in an opposite order. The difference between their Gibbs energy reaches the maximum at ~0.85wt% B, corresponding to the largest driving force for early formed M_7C_3 to transform to $M_{23}C_6$, facilitating the formation of core-shell structured carbides.
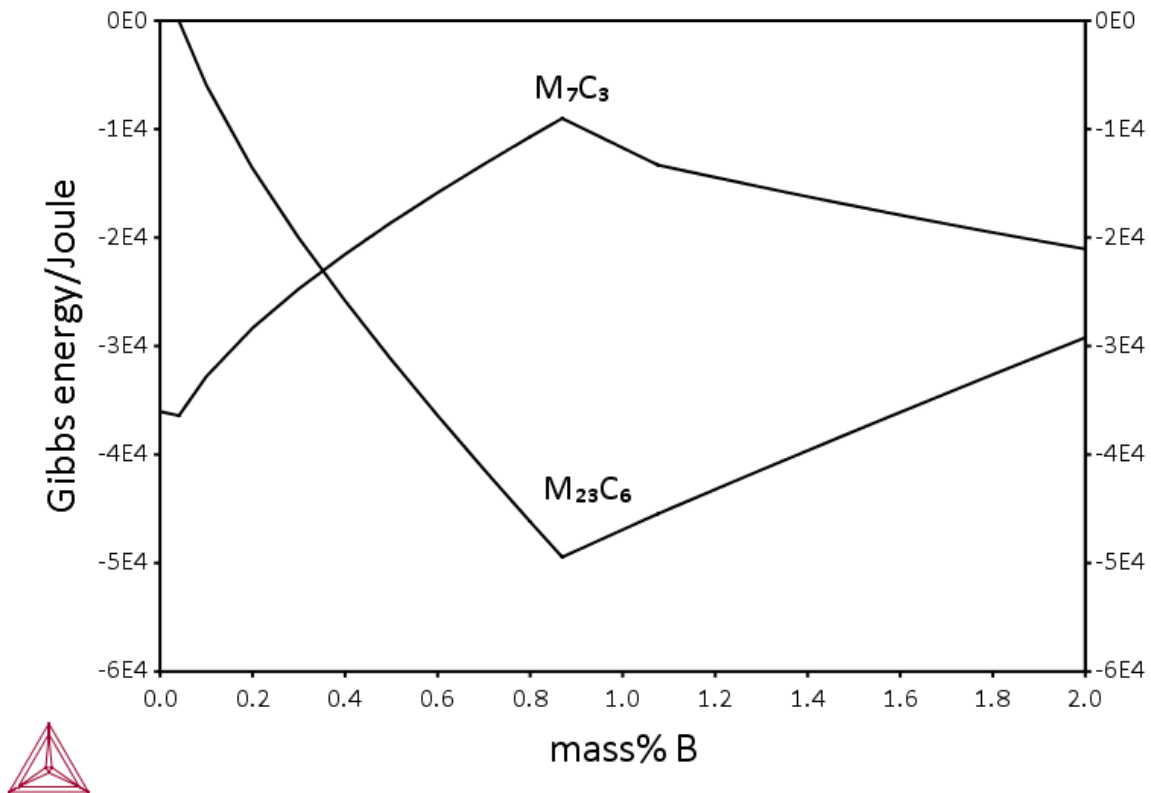
Fig.14 *Gibbs energies of M_7C_3 and $M_{23}C_6$ in Fe45Cr5CB alloy at 900°C, calculated with the boron concentration range from 0 to 2wt%.*

3.2.2 Experimental verification - microstructure

The cast irons with and without B addition under study were fabricated using an arc furnace as described earlier. SEM was employed to characterize the microstructure of the fabricated cast irons under both as-cast and annealing conditions (see Fig.15), respectively. Volume fraction of carbides was analyzed by image binarization. Results of EDS analysis are presented in Table 1. Since boron is a light element, EDS is unable to detect it. Thus, data of B is not included in Table 1. In general, the specimens under study show bulky hexagonal or rod-like M_7C_3 carbides, depending on the orientation of sample cutting, and fine eutectic carbides embedded in the ferrous matrix. Eutectic carbides can be M_7C_3 or $M_{23}C_6$, depending on the chemical composition of the alloy. In the as-cast Fe45Cr3C alloy (Fig.15a and Fig.15b), both primary and eutectic carbides are M_7C_3; whereas under the annealing condition (Fig.15c), $M_{23}C_6$ phase is detected mainly as eutectic carbides along with previuosly formed primary and eutectic M_7C_3 during the solidification process. The observation is in accordance with the calculated phase diagram (Fig.12a), which shows that the Fe45Cr3C alloy is in a two-phase region of $M_{23}C_6+\alpha$-Fe when in equilibrium at the annealing temperature. Similar to the as-cast Fe45Cr3C alloy, Fe45Cr5C alloy consists of M_7C_3 and iron-based matrix (Fig.15g, Fig.15h and Fig.15i). With the higher carbon content at 5wt%, this alloy has a larger volume fraction of carbides, compared to that of Fe45Cr3C alloy.

Fig.15d, Fig.15e and Fig.15f illustrate the microstructure of the Fe45Cr3C1.1B alloy, in which the dark grey carbides are M_7C_3, and the light grey shell and eutectic carbides are $M_{23}C_6$. Due to the high solidification rate, the $M_7C_3 \rightarrow M_{23}C_6$ transformation shown in Fig.12b may be only partially proceeded, thus resulting in the formation of

core-shell structured carbides. For the sample annealed at 650°C, equilibrium phases include M_7C_3 and $M_{23}C_6$; thereby there is no significant change in microstructure observed before and after heat treatment. In the case of FeCr5C0.8B alloy, its microstructure is similar to that of the FeCr5C alloy when in the as-cast condition. However, core-shell structured carbides formed in the annealed sample. As temperature reaches 900°C, the equilibrium phases are composed of γ-Fe, M_7C_3 and B-doped $M_{23}C_6$. While the initial matrix+ M_7C_3 colony offers prerequisite [13], high temperature provides thermal energy for $M_{23}(C, B)_6$ nucleation, leading to the formation of core-shell structured carbides. The equilibrium state of FeCr5C0.8C alloy at 900°C was calculated, which shows that $M_{23}(C, B)_6$ contains 42.80at% Fe, 36.51at% Cr, 16.58at% C and 4.11at% B, while M_7C_3 consists of 17.79at% Fe, 52.21at% Cr, 29.62at% C and 0.38at% B. According to the thermodynamic calculation, boron is mainly distributed in $M_{23}(C, B)_6$. Comparing the Cr/Fe ratio of $M_{23}(C, B)_6$ and M_7C_3 from EDS analysis (Table 1) and thermodynamics calculation, the equilibrium state is reached after heat treatment.
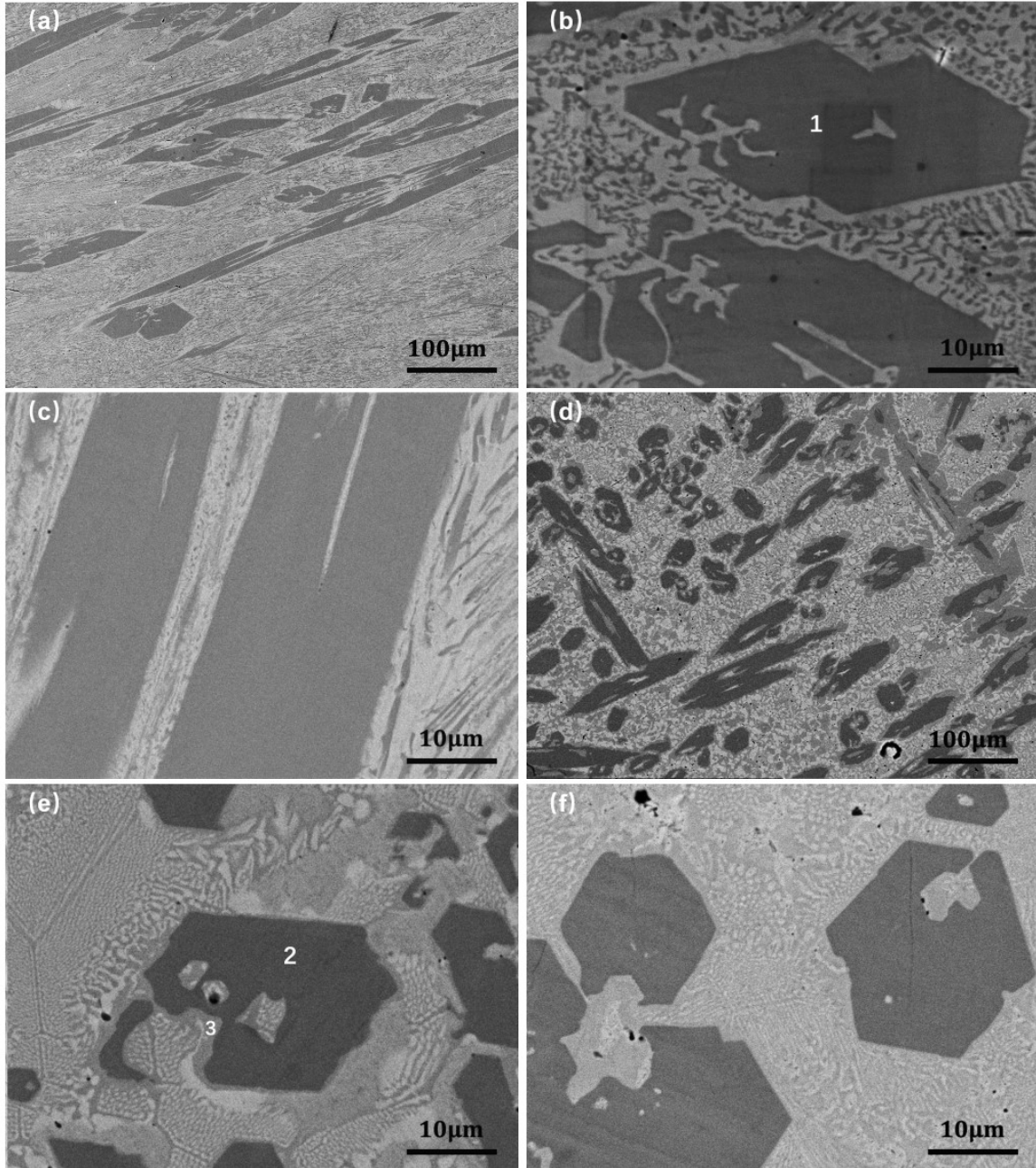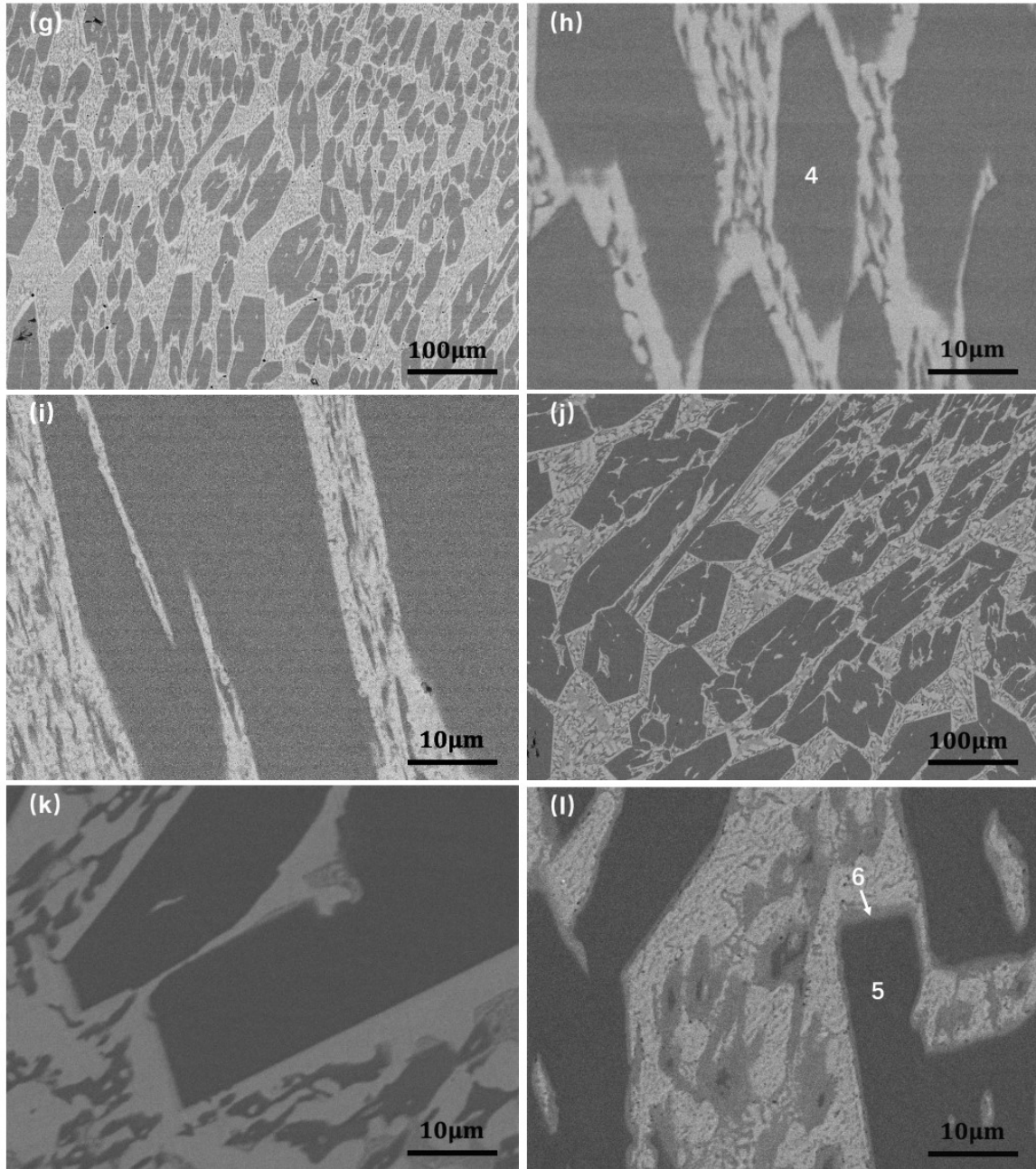
Fig.15 *SEM images of microstructure: (a) and (b) as-cast Fe45Cr3C alloy, (c) Fe45Cr3C alloy annealed at 650℃ for 4 hours, (d) and (e) as-cast Fe45Cr3C1.1B alloy, (f) Fe45Cr3C1.1B alloy annealed at 650℃ for 4 hours, (g) and (h) as-cast Fe45Cr5C alloy, (i) Fe45Cr5C alloy annealed at 900℃ for 4 hours, (j) and (k) as-cast Fe45Cr5C0.8B alloy, (l) Fe45Cr5C0.8B alloy annealed at 900℃ for 4 hours. Core-shell structured carbides are observed in Fig.15d, Fig.15e, Fig.15f and Fig.15l.*

Table 1 - EDS results of M_7C_3 and $M_{23}C_6$ in Fe45Cr3C, Fe45Cr3C1.1B, Fe45Cr5C and Fe45Cr5C0.8B alloy

	Fe(at%)	Cr(at%)	C(at%)
1	17.59	51.13	31.28
2	15.65	56.18	28.17
3	36.68	42.67	20.65
4	15.70	48.38	35.92
5	17.26	48.39	34.36
6	38.94	32.20	28.86

XRD phase analysis was carried out for the sample alloys. As shown in Fig.16, the matrix of as-cast alloys is ferrite and/or retained austenite. In all heat-treated (annealed) samples, only ferrite is detected. According to Fig.16a, the heat-treated FeCr3C contains a small amount of $M_{23}C_6$ in addition to the matrix and M_7C_3, which is consistent with the SEM observation and thermodynamics calculation. FeCr3C1.1B alloy consists of more $M_{23}C_6$ along with the ferrous matrix and M_7C_3, indicating that boron addition promotes the formation of $M_{23}C_6$. As Fig.16b illustrates, results of the phase analysis are consistent with the phase calculation using Thermo-Calc (Fig.12a and Fig.12c). After annealing at 900°C for 4 hours, $M_{23}C_6$ formed with a decrease in the amount of M_7C_3 (encircled in Fig.16b). With regards to the calculated phase diagram (Fig.12c) and SEM images (Fig.15j, Fig.15k and Fig.15l), M_7C_3 is the parental phase from which $M_{23}C_6$ is transformed, leading to the formation of core-shell structured carbides.

(a)

(b)
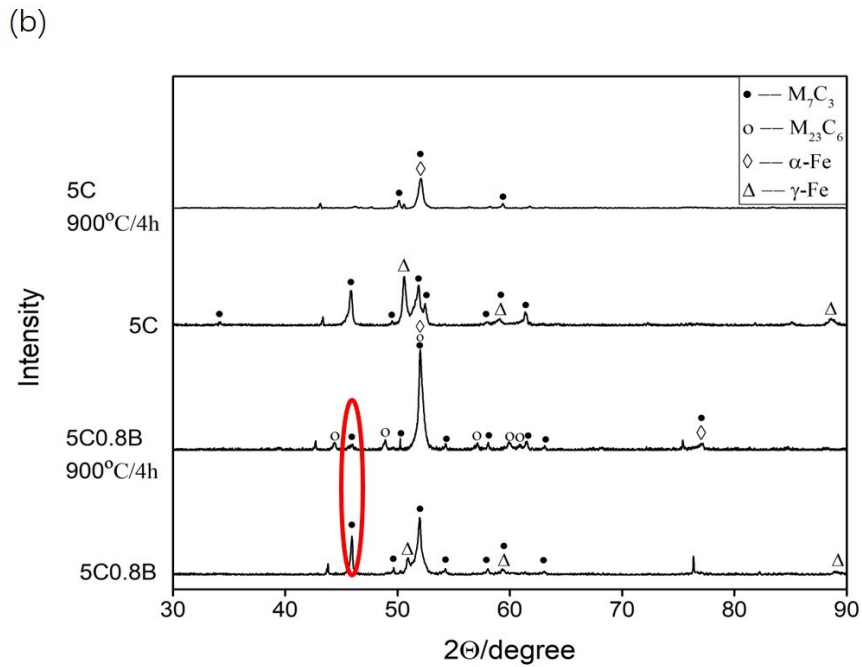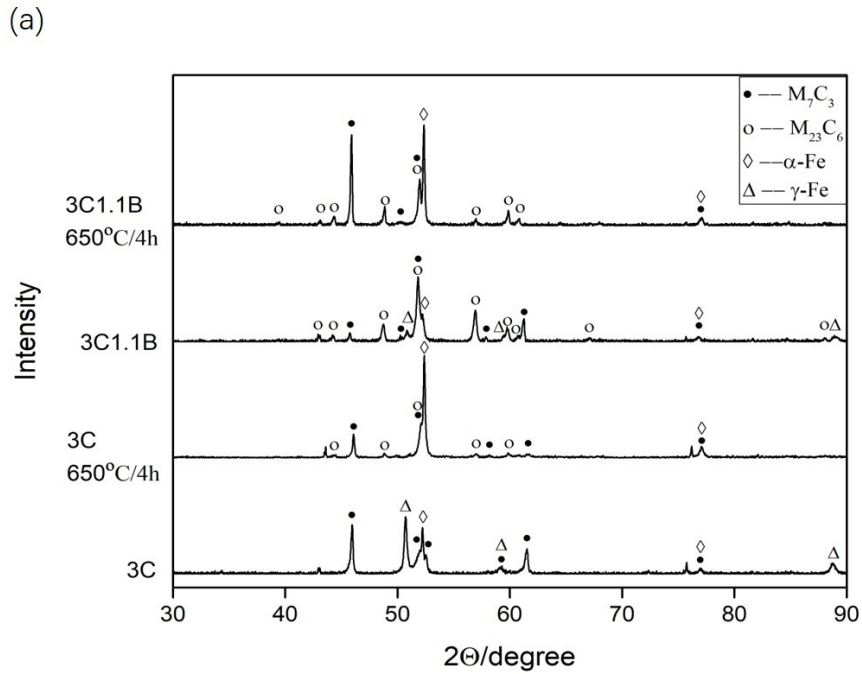
Fig.16 *XRD patterns for (a) Fe45Cr3C, Fe45Cr3C1.1B, (b) Fe45Cr5C and*

Fe45Cr5C0.8B alloy (The red circle indicates a decrease in the amount of

M₇C₃ after annealing).

Since EDS is unable to detect light elements such as boron, Auger microscope in backscattered imaging mode was applied to the Fe45Cr5C0.8B alloy. By mapping the microstructure, distributions of individual elements are illustrated in Fig.17. The color indicates the concentration of elements. For instance, red color represents high concentration and blue color represents lower one. According to Fig.17, the core carbide is enriched with chromium and low in iron, while the shell carbide shows an opposite trend. Besides, the carbon map presented in Fig.17d shows that the shell has a lower concentration of carbon than the core, indicating that the core is M_7C_3 and the shell is $M_{23}(C,B)_6$. From Fig.17e, boron tends to segregate in the shell carbide area and has lower concentration inside the core and the matrix. Point chemical composition analysis shows that about 4.4at% of boron is detected in $M_{23}(C,B)_6$, in accordance with the calculated composition of $M_{23}(C,B)_6$ in Fe45Cr5C0.8B alloy.
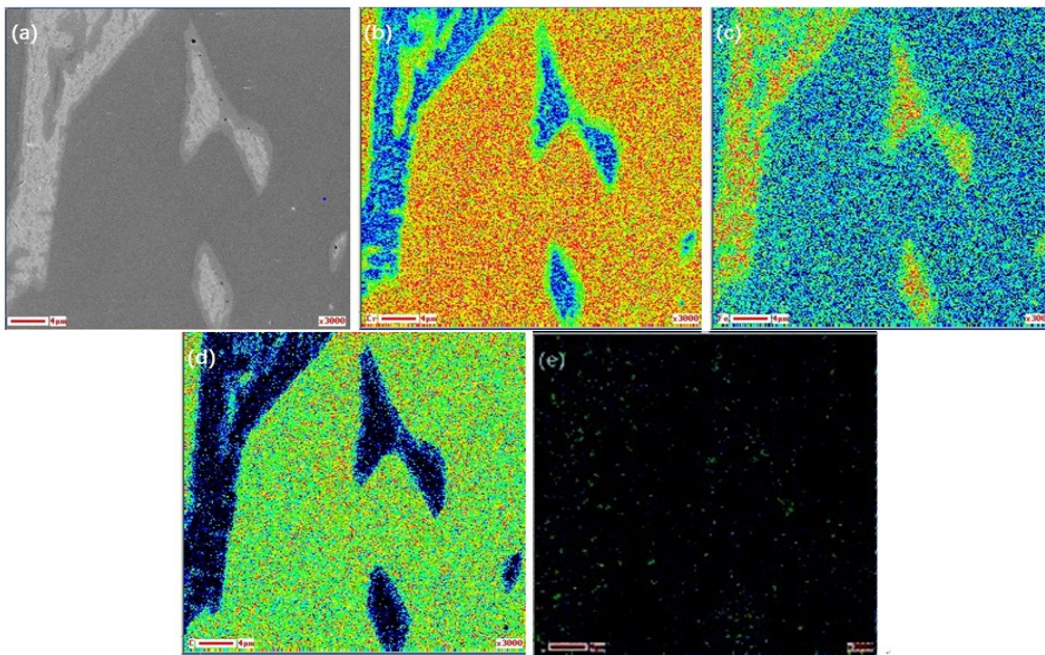
Fig.17 *AES images of Fe45Cr5C0.8B alloy: (a) backscattered image of tested area, and maps of element (b) Cr, (c) Fe, (d) C and (e) B.*

3.2.3 Effect of B on formation of core-shell structured carbides: first-principles calculations

3.2.3.1 Stability and mechanical properties of $M_{23}C_6$ and $M_{23}(C, B)_6$

As a transitional layer between the harder M_7C_3 core and softer ferrous matrix, the $M_{23}C_6$ shell benefits the wear resistance of HCCIs [7, 12]. Since B basically stays in the shell region ($M_{23}C_6$), it is of interest to see how the formation and mechanical properties of $M_{23}C_6$ are influenced. First-principles calculation was employed to calculate the formation energy and evaluate the mechanical properties of $M_{23}C_6$ and B-doped $M_{23}(C, B)_6$. $M_{23}C_6$ has a cubic crystal structure in which exist four equivalent metal sites [110]. The Wyckoff positions are site 4a (0, 0, 0), site 8c (0.25, 0.25, 0.25), site 32f (0.385, 0.385, 0.385) and site 48h (0, 0.165, 0.165). The crystal structure of $M_{23}C_6$ is illustrated in Fig.18. Based on the EDS analysis (Table 1) and thermodynamics calculations, the experimental and calculated Cr/Fe ratios of $M_{23}(C, B)_6$ in Fe45Cr5C0.8B alloy are 38.94:32.20 and 42.80:36.51 respectively. Thus, the atomic ratio of calculated $M_{23}C_6$ is set to be Fe:Cr:C=13:10:6. From AES point analysis, the boron content in $M_{23}(C, B)_6$ is 4.4at%. Therefore, one C atom is substituted by B atom in the $M_{23}C_6$. After geometry optimization, the lattice parameter of $Fe_{13}Cr_{10}C_6$ is a=b=c=10.436Å, α=β=γ=90°, while the lattice parameter of $Fe_{13}Cr_{10}C_5B$ is a=c=10.356Å, b=10.388Å, α=γ=89.849°, β=90.302°, which means the lattice slightly distorts when boron is doped.
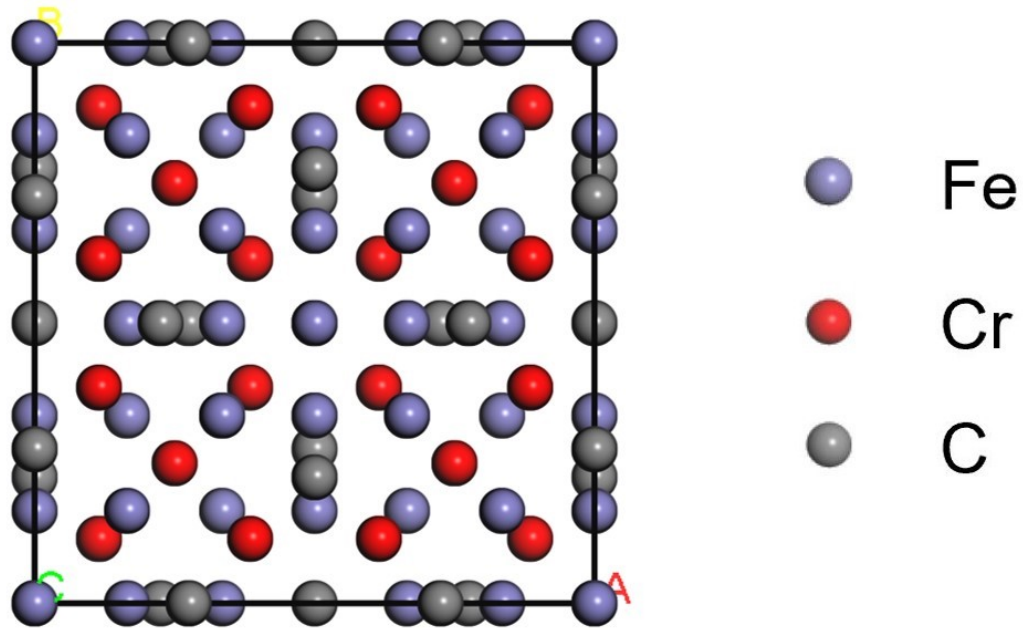
Fig.18 *Crystal structure of M$_{23}$C$_6$.*

To demonstrate how boron addition influences the formation of M$_{23}$C$_6$, the formation energies of Fe$_{13}$Cr$_{10}$C$_6$ (ΔU_1) and Fe$_{13}$Cr$_{10}$C$_5$B (ΔU_2) were calculated using the following equations:

$$\Delta U_1 = \frac{E_{total} - [13E_i(Fe) + 10E_i(Cr)+6E_i(C)]}{29} \tag{3.1}$$

$$\Delta U_2 = \frac{E_{total} - [13E_i(Fe) + 10E_i(Cr)+5E_i(C)+E_i(B)]}{29} \tag{3.2}$$

where E_{total} is the total energy of M$_{23}$C$_6$, $E_i(Fe)$, $E_i(Cr)$, $E_i(C)$ and $E_i(B)$ are the energy per atom of bulk Fe, Cr, C and B, respectively. Calculated ΔU_1 and ΔU_2 equal to -9.63meV and -31.85meV, respectively, indicating adding boron in M$_{23}$C$_6$ leads to higher stability of M$_{23}$(C, B)$_6$.

In order to investigate how boron addition modifies the mechanical properties of $M_{23}C_6$, the elastic constants C_{ij} of $Fe_{13}Cr_{10}C_6$ and $Fe_{13}Cr_{10}C_5B$ were calculated and are listed in Table 2. Bulk modulus B_v, shear modulus G_v, Young's modulus E [111] are derived from elastic constants by the following equations and presented in Table 3:

$$B_v = \frac{1}{9}[C_{11} + C_{22} + C_{33} + 2(C_{12} + C_{13} + C_{23})] \tag{3.3}$$

$$G_v = \frac{1}{15}[C_{11} + C_{22} + C_{33} + 3(C_{44} + C_{55} + C_{66}) - (C_{12} + C_{13} + C_{23})] \tag{3.4}$$

$$E = \frac{9B_vG_v}{3B_v + G_v} \tag{3.5}$$

The bulk modulus represents the ability of a material to resist volume change under pressure. The B_v of $Fe_{13}Cr_{10}C_5B$ is larger than that of $Fe_{13}Cr_{10}C_6$. Young's modulus E describes the stiffness of materials. E of $Fe_{13}Cr_{10}C_5B$ is 330.23GPa, which is about 18GPa larger than the E of $Fe_{13}Cr_{10}C_6$ but 54GPa smaller than reported Young's modulus of $Fe_3Cr_4C_3$ (384GPa) [63]. The increased E of $M_{23}C_6$ by the B addition indicates that B increases the atomic bonding, compared to that of non-doped $M_{23}C_6$ carbide. It is particularly worth noting that B increases the B_v/G_v ratio. This ratio is related to the brittleness or ductility of materials [63]. The higher the B_v/G_v ratio, the higher the ductility or flexibility. As shown in Table 3, the B addition increases the B_v/G_v ratio of $M_{23}C_6$ by about 30%, meaning that $(Fe, Cr)_{23}(C, B)_6$ is more flexible than $(Fe, Cr)_{23}C_6$.

Thus, the boron addition in $Fe_{13}Cr_{10}C_6$ increases not only Young's modulus of $M_{23}C_6$ carbide, corresponding to stronger atomic binding, but also its ductility or

flexibility. As demonstrated by ab initio calculations [17], M-B bonding is stronger than M-C bonding, which may explain the positive effect of B on the atomic bonding strength.

Table 2 - Calculated elastic constants C_{ij} of $Fe_{13}Cr_{10}C_6$ and $Fe_{13}Cr_{10}C_5B$ (GPa)

	C_{11}	C_{12}	C_{13}	C_{22}	C_{23}	C_{33}	C_{44}	C_{55}	C_{66}
$Fe_{13}Cr_{10}C_6$	383.22	135.11	134.24	383.22	134.24	384.09	124.05	123.19	123.19
$Fe_{13}Cr_{10}C_5B$	455.58	201.65	208.71	451.51	198.20	451.74	125.87	129.88	125.47

Table 3 - Calculated mechanical properties of $Fe_{13}Cr_{10}C_6$ and $Fe_{13}Cr_{10}C_5B$ (GPa)

	B_v	G_v	B_v/G_v	E
$Fe_{13}Cr_{10}C_6$	217.52	123.88	1.76	312.35
$Fe_{13}Cr_{10}C_5B$	286.22	126.26	2.27	330.23

3.2.3.2 Effect of boron on the formation of core-shell structured carbides

In order to illustrate why boron promotes the formation of $M_{23}C_6$ at the interface of the matrix and M_7C_3, instead of forming $M_{23}C_6$ inside the matrix, interfacial energies of $M_{23}C_6/M_7C_3$ and $M_{23}C_6/Fe$ interfaces with or without boron addition are worth being investigated. Interfacial energy is the energy needed to increase a unit area of interface. The lower the value of interfacial energy is, the easier the formation of the interface. Interfacial energy can be described as follows [63]:

$$\gamma = \sigma_1 + \sigma_2 - W_{ad} \tag{3.6}$$

where, γ is the interfacial energy, σ_1 and σ_2 are surface energies of surface 1 and surface 2, respectively, W_{ad} is the work of adhesion.

The work of adhesion (W_{ad}) is the work needed to separate two adjacent phases by destroying their interface and creating two free surfaces having surface energies of σ_1 and σ_2, respectively. The larger the value of W_{ad}, the stronger the interfacial bonding strength. W_{ad} [63] is represented as:

$$W_{ad} = \frac{1}{A}\left(E_1 + E_2 - E_{1/2}\right) \tag{3.7}$$

E_1 and E_2 are the energies of fully relaxed slab 1 and slab 2, respectively. $E_{1/2}$ is the energy of the fully relaxed interface, A is the area of interface.

To investigate the effect of B on $M_{23}C_6/M_7C_3$ interface, we chose $Cr_4Fe_3C_3$ for the calculation, since previous studies demonstrate that M_7C_3 carbide is more stable when the Cr/Fe ratio is 4:3 [6, 74]. According to previous TEM characterization [11], which showed the orientation relationships between $M_{23}C_6$ and M_7C_3, we chose the (1 1 1) plane of $M_{23}C_6$ and (1 $\bar{1}$ 0 0) plane of M_7C_3 to form a $M_{23}C_6//M_7C_3$ interface. A $Fe_{13}Cr_{10}C_6$ supercell with (1 1 1) surface and a $Cr_4Fe_3C_3$ supercell with (1 $\bar{1}$ 0 0) surface were combined to build the interface as illustrated in Fig.19. Values of W_{ad} for $Fe_{13}Cr_{10}C_6/Cr_4Fe_3C_3$ interface and that of $Fe_{13}Cr_{10}C_5B/Cr_4Fe_3C_3$ interface were calculated, which are $3.51 J/m^2$ and $3.89 J/m^2$, respectively. The result indicates that with the boron addition, the interfacial bonding between $Fe_{13}Cr_{10}C_6$ and $Cr_4Fe_3C_3$ carbides become stronger, implying that $M_{23}C_6$ carbide preferentially forms on M_7C_3.
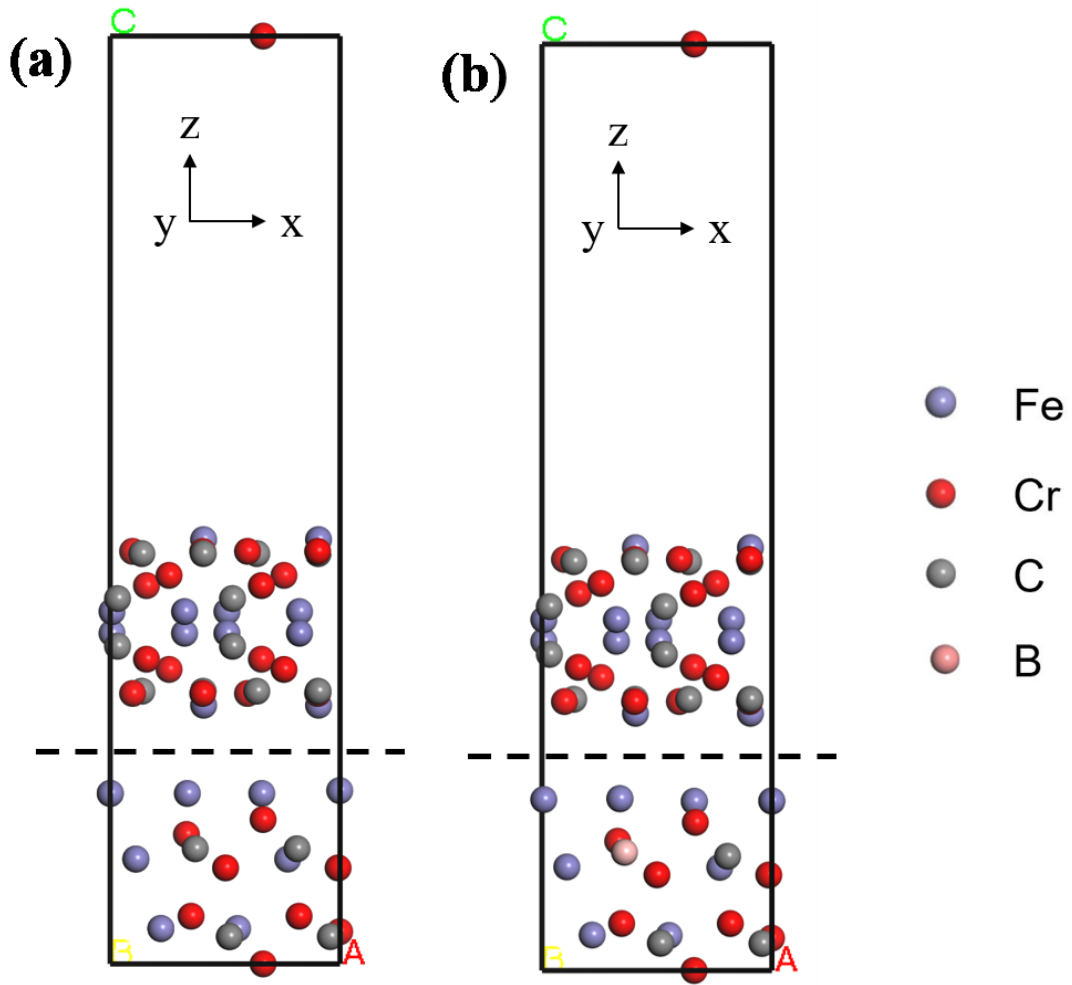
Fig.19 *Models of (a) Fe$_{13}$Cr$_{10}$C$_6$/Cr$_4$Fe$_3$C$_3$ and (b) Fe$_{13}$Cr$_{10}$C$_5$B/Cr$_4$Fe$_3$C$_3$ interfaces*

before relaxation.

According to previous studies [112], the α-Fe/M$_{23}$C$_6$ interface has the orientation

relationship: $(1\ 1\ 0)_\alpha//(1\ 1\ 1)_{M23C6}$. A 1×1 Fe$_{13}Cr_{10}C_6$ supercell with $(1\ 1\ 1)$ surface and a

2×3 Fe supercell with $(1\ 1\ 0)$ surface were chosen to form an interfacial system. The

interfacial models are illustrated in Fig.20, in which the dashed line represents the

Fe$_{13}$Cr$_{10}$C$_6$ $(1\ 1\ 1)$/Fe $(1\ 1\ 0)$ interface. According to Eq. (3.7), W_{ad} of Fe$_{13}$Cr$_{10}$C$_6$/Fe

interface was calculated which is equal to 3.95J/m^2, whereas that of Fe$_{13}$Cr$_{10}$C$_5$B/Fe

interface is 3.36J/m², implying that the B makes the $M_{23}C_6$ grow on M_7C_3 instead of in the matrix more preferentially.
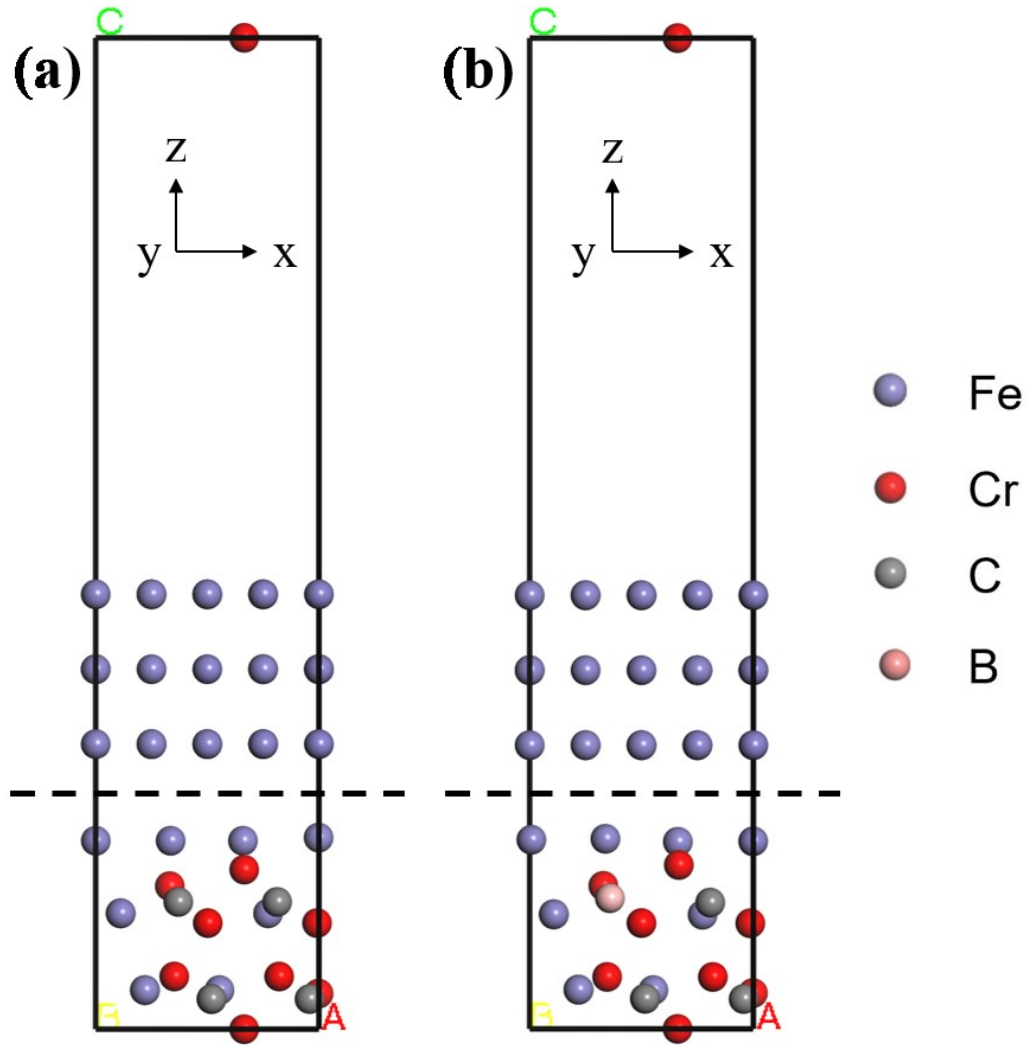
Fig.20 Models of (a) Fe₁₃Cr₁₀C₆/Fe and (b) Fe₁₃Cr₁₀C₅B/Fe interfaces before relaxation

In order to calculate interfacial energies of $M_{23}C_6/M_7C_3$ and $M_{23}C_6/Fe$ interfaces with or without boron, surface energies of $Fe_{13}Cr_{10}C_6$ (1 1 1) slab, $Fe_{13}Cr_{10}C_5B$ (1 1 1) slab, $Cr_4Fe_3C_3$ (1 $\bar{1}$ 0 0) slab and Fe (1 1 0) slab are needed. Since the main goal is to

compare the interfacial energy with or without boron, the surface energies of $Cr_4Fe_3C_3$ ($\bar{1}$ 0 0) slab and Fe (1 1 0) slab for analyzing the interfaces with $Fe_{13}Cr_{10}C_6$ and $Fe_{13}Cr_{10}C_5B$ are the same, which have no influence on the comparison of interfacial energies. Thus, only the surface energies of $Fe_{13}Cr_{10}C_6$ slab and $Fe_{13}Cr_{10}C_5B$ slab were calculated. The surface energy can be given as the following equation [113]:

$$\sigma = \frac{1}{2A}(E_{slab} - nE_{bulk}) \qquad (3.8)$$

where, E_{slab} denotes the energy of the slab after fully relaxation, n is the number of $M_{23}C_6$ in the slab, E_{bulk} is the energy of bulk $M_{23}C_6$, A is the surface area. According to Fig.19 and Fig.20, the two surfaces of $M_{23}C_6$ are not equal; thus the calculated σ is an average surface energy. σ of $Fe_{13}Cr_{10}C_6$ slab is 3.05 J/m^2 while that of $Fe_{13}Cr_{10}C_5B$ slab is 3.13 J/m^2.

The surface energy of $Fe_{13}Cr_{10}C_6$ slab is 0.08 J/m^2 smaller than that of $Fe_{13}Cr_{10}C_5B$ slab, whereas the W_{ad} of the $Fe_{13}Cr_{10}C_6/Cr_4Fe_3C_3$ interface is 0.38 J/m^2 smaller than that of $Fe_{13}Cr_{10}C_5B/Cr_4Fe_3C_3$ interface. The W_{ad} of the $Fe_{13}Cr_{10}C_6/Fe$ interface is 0.59 J/m^2 larger than that of $Fe_{13}Cr_{10}C_5B/Fe$ interface. According to Eq. (3.6), the interfacial energy of $M_{23}C_6/M_7C_3$ interface becomes smaller and that of $M_{23}C_6/Fe$ interface becomes larger with the boron addition, indicating that boron addition promotes the formation of $M_{23}C_6/M_7C_3$ interface and reduces the probability of forming $M_{23}C_6$ in the matrix. It may explain why the boron addition can prompt the formation of core-shell structured carbides instead of forming $M_{23}C_6$ in the matrix.

3.3 Conclusions

The core-shell structured carbide in high-Cr cast irons (HCCIs) has stronger interfacial bonding with the ferrous matrix and is thus beneficial to the wear resistance of HCCIs. However, such configured carbide is not always present in HCCIs. We conducted thermodynamic analysis to investigate the possibility of promoting the formation of core-shell structured carbides through alloying elements. In this study, the effect of boron on the formation of core-shell structured carbides was investigated through thermodynamic calculations in combination with experimental verification and first-principles calculations. The following conclusions are drawn from the study.

1. In Fe45Cr3C alloy, no core-shell structured carbide exists. After 1.1wt% boron addition, core-shell structured carbides are formed due to non-equilibrium solidification. In Fe45Cr5C alloy and quenched Fe45Cr5C0.8B alloy, phase constituents are only the matrix and M_7C_3. However, $M_{23}(C, B)_6$ forms at the M_7C_3/matrix interface when FeCr5C0.8B alloy was annealed, resulting in the formation of core-shell structured carbides.

2. Boron addition can stabilize $M_{23}(C, B)_6$ by decreasing its Gibbs energy. The driving force for M_7C_3 transforming to $M_{23}(C, B)_6$ is maximized when the concentration of added B is around 0.85wt% in the Fe45Cr5C alloy.

3. First-principles calculations demonstrate that the B addition increases both the mechanical strength and flexibility of $M_{23}C_6$ carbide, evidenced by the improvement in the properties of $Fe_{13}Cr_{10}C_5B$ in comparison with $Fe_{13}Cr_{10}C_6$.

4. The boron addition enhances the interfacial bonding strengths of $Fe_{13}Cr_{10}C_6/Cr_4Fe_3C_3$. As a result, the probability of forming the core-shell structured carbides is increased by the B addition, thus benefiting the resistance to interfacial failure.

Chapter 4 Modification on mechanical properties of (Fe, Cr, X)$_7$C$_3$ (X=W, V) in hypereutectic HCCIs

4.1 Methods

4.1.1 Materials and characterization

The material used for this study is a high chromium cast iron containing 5wt% C and 40wt% Cr, balanced by Fe. In order to modify its carbides, base materials were re-melted to add alloying element, 18wt% W and 5wt% V, respectively. Samples were made using the arc furnace, then cut into specimens. Samples were wet grounded with SiC papers (up to 2000 grit) and polished by 1 μm alumina powder. Before AFM analysis, the specimens were etched with picral solution and cleaned in ethanol.

The microstructure of specimens was characterized using SEM (Tescan Vega-3) in backscattered electron mode and compositions of each phase were measured by equipped EDS (Energy Dispersive Spectroscopy). The local electron work function and the Young's modulus of specimens were mapped using a Bruker MultiMode AFM 8 with KPFM capability. All local property maps were obtained in the same area.

4.1.2 Computational methods

The CALPHAD method was utilized via Thermo-Calc [106] with TCFE6 database to investigate the solubility of alloying elements, W and V, in M$_7$C$_3$. With consideration of the solubility, the chemical compositions of the tested materials were determined to be Fe-40wt%Cr-5wt%C-18wt%W and Fe-40wt%Cr-5wt%C-5wt%V.

First-principles calculations were conducted with the density functional theory (DFT) as implemented in the Vienna ab initio simulation package (VASP) [107, 108]. The exchange-correlation energy was calculated within the generalized gradient approximation (GGA) of Perdew-Burke-Ernzerhof (PBE) [109]. As shown in Fig.21, M_7C_3 has a hexagonal close packed crystal structure with space group P63mc. Three equivalent metal sites, M1, M2, M3 and one carbon site are contained in M_7C_3. In the calculation of formation energy, cohesive energy and modulus, a cutoff energy for plane-wave basis was set to be 600 eV and a k-point grid of 7×7×9 was utilized. For calculation of electron work function, bulk M_7C_3 was cleaved along the (0 0 0 1) plane and a 15 Å vacuum layer was added as shown in Fig.21(c). Then, the slab was calculated with a k-point sampling of 7×7×1. The self-consistency was achieved when electronic convergence reached 10^{-5} eV and the Hellmann-Feynman forces on each atom were less than 0.01eV/Å.
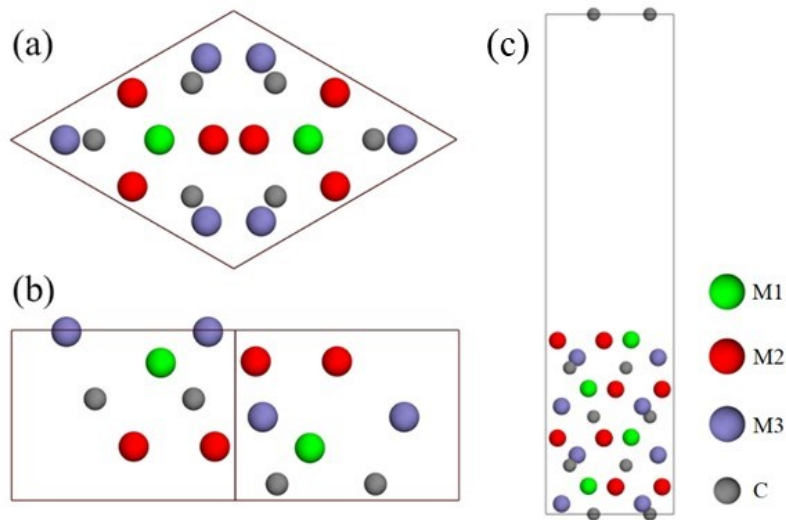
Fig.21 *Crystal structure of M_7C_3: (a) and (b) are the top and side view of bulk M_7C_3 unit cell, (c) is the (0 0 0 1) slab of M_7C_3.*

4.2 Results and discussion

4.2.1 Thermodynamics analysis

To determine the mass percentage of alloying elements added to the materials, the solubility of W and V in M_7C_3 was calculated at 1000°C as illustrated in Fig.22. As shown in Fig.22a, the solute W in M_7C_3 is less than 1.5wt% when W addition in the specimen is smaller than 13wt%, which may be difficult to be detected by EDS. Thus, a large amount of W needs to be added. While for V, the solubility of V in M_7C_3 is higher than W, so that less V is necessary to be added in the specimen. In this study, 18wt% W and 5wt% V are added, respectively. According to the thermodynamics calculation, 3.18wt% W and 8.61wt% V can be dissolved in M_7C_3.
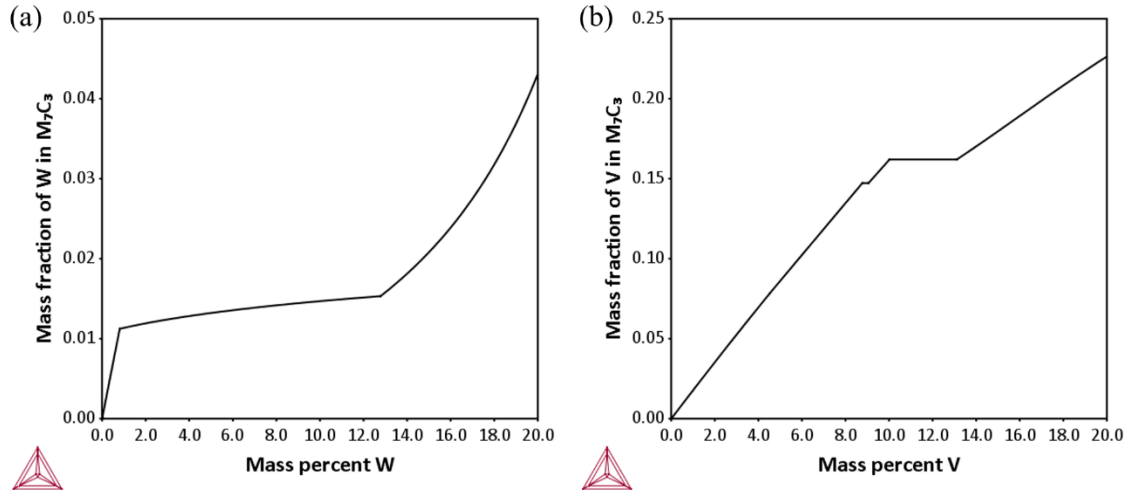
Fig.22 *(a) Mass fraction of W in M_7C_3 as a function of nominal mass percentage of W in the cast irons; (b) mass fraction of V in M_7C_3 as a function of nominal mass percentage of V in the cast irons.*

4.2.2 Microstructural observation

The microstructures of Fe-40wt%Cr-5wt%C-18wt%W alloy and Fe-40wt%Cr-5wt%C-5wt%V alloy are shown in Fig.23. The compositions of $(Fe, Cr, X)_7C_3$ carbides were analyzed by EDS and listed in Table 4. Both alloys present hypereutectic microstructure, which is a combination of primary M_7C_3 carbides and (matrix+M_7C_3) eutectic colony. As shown in Table 4, the atomic percentage of tungsten in the matrix is 8.25%, while that in M_7C_3 is 2.92%. The atomic percentage of vanadium in the matrix is only 1.41%, whereas that in M_7C_3 is 6.79%. Both W and V are capable of forming the complex $(Fe, Cr, X)_7C_3$ carbides. However, V exhibits the higher capability to be dissolved in M_7C_3. The value of EDS results is different from the thermodynamics calculation since the samples are in as-cast condition which is a non-equilibrium state. Nevertheless, the trend in solubility is similar.
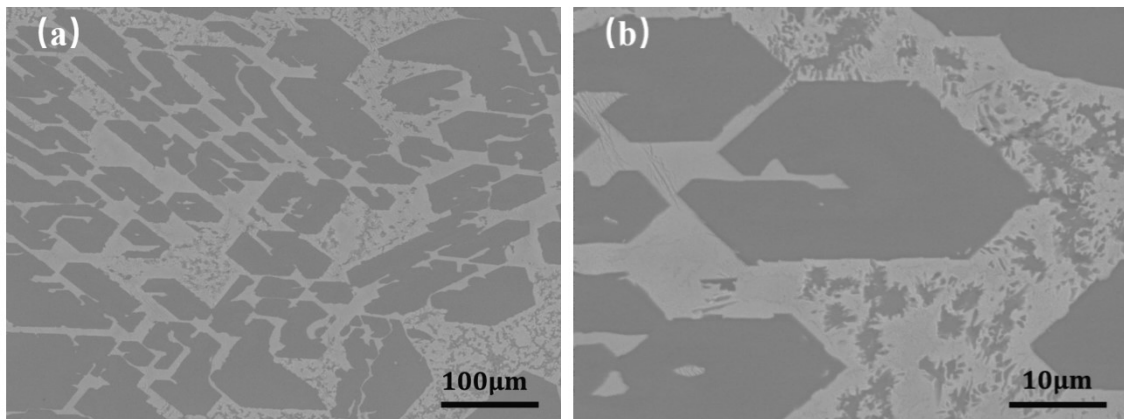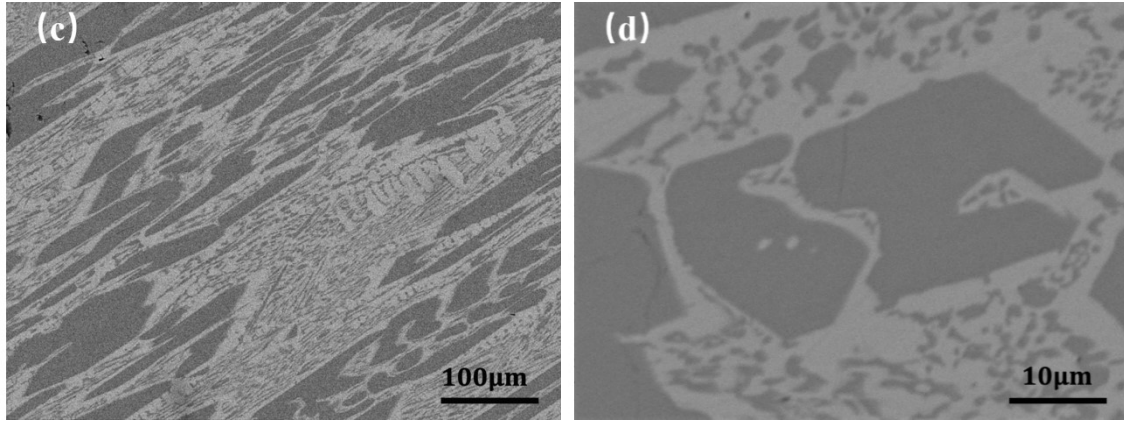
Fig.23 SEM images of microstructure: (a) and (b) Fe-40wt%Cr-5wt%C-18wt%W alloy; (c) and (d) Fe-40wt%Cr-5wt%C-5wt%V alloy.

Table 4 - EDS results of matrix and M_7C_3 in Fe-40wt%Cr-5wt%C-18wt%W and Fe-40wt%Cr-5wt%C-5wt%V alloy, respectively.

		Fe(at%)	Cr(at%)	C(at%)	W(at%)	V(at%)
Fe-40wt%Cr-5wt%C-18wt%W	Matrix	53.25	19.83	18.66	8.25	-
	M_7C_3	14.52	48.43	34.12	2.92	-
Fe-40wt%Cr-5wt%C-5wt%V	Matrix	76.10	22.49	0	-	1.41
	M_7C_3	17.00	45.41	30.80	-	6.79

4.2.3 AFM mapping

In order to measure the local electron work function and Young's modulus, a multimode AFM was applied to map the properties and obtain quantitative results. Representative maps of topography, work function and Young's modulus are illustrated

in Fig.24. The measured work function and modulus of M_7C_3 are presented in Table 5. In the topography map in Fig.24, the bright phase is M_7C_3 while the dark phase is the matrix. In the work function map, the brighter the phase is, the higher the work function. The modulus map shows a similar trend. Thus, the AFM maps indicate that carbides have higher work function and modulus than the matrix. According to Table 5, W-doped M_7C_3 exhibits higher EWF and modulus than $(Fe, Cr)_7C_3$, while V-doped M_7C_3 has lower EWF and modulus than $(Fe, Cr)_7C_3$, which brings up a hypothesis that EWF is correlated to the mechanical strength for the carbide.
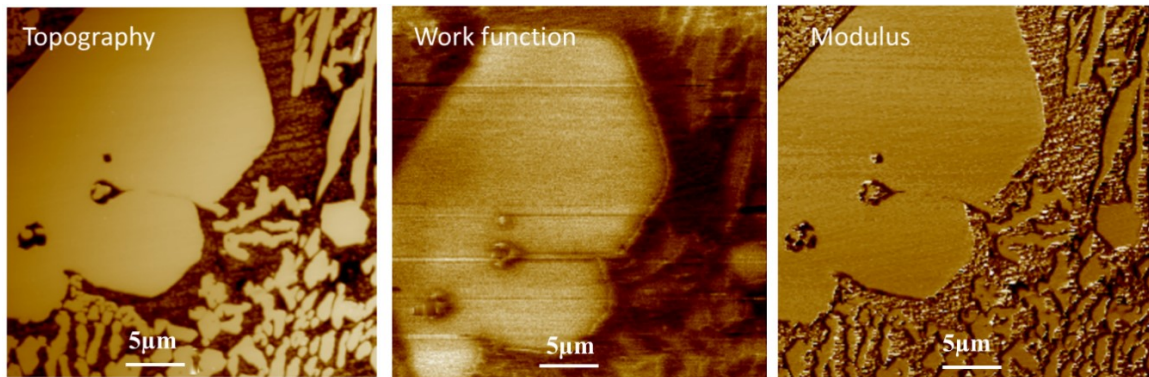
Fig.24 Representative AFM maps of topography, electron work function and modulus of a cast iron sample.

Table 5 - Measured work function and Young's modulus of M_7C_3 with and without metallic substitutions

	Fe-40Cr-5C	Fe-40Cr-5C-18W	Fe-40Cr-5C-5V
Work function (eV)	4.61	4.838	4.545
Modulus (Gpa)	358.84	412.25	341.32

4.2.4 First-principles calculations

According to the AFM analysis results, substitutional metallic elements in M_7C_3 vary the EWF and modulus of carbides. A hypothesis that the mechanical strength of carbides is correlated to the EWF is proposed. In order to prove the hypothesis, a first-principles method was implemented to first analyze the stability of $(Fe, Cr, X)_7C_3$, then calculate their EWF, as well as Young's modulus, and compare those calculated results to experimental observations.

4.2.4.1 Stability of $(Fe, Cr, X)_7C_3$

In this study, one W or V atom substitutes one Fe atom in $Fe_4Cr_3C_4$ carbide. The reason to replace Fe instead of Cr is that the cohesive energy of M_7C_3 decreases with increasing Cr, which indicates that Cr is more tightly bonded than Fe. It is also in agreement with the studies conducted by Yamamoto et al [24]. To determine the stability of those carbides, formation energies and cohesive energies were calculated at temperature of 0 K and pressure of 0 Pa. The formation energy (ΔU) can be described as:

$$\Delta U = \frac{E_{total} - [2E_i(M1) + 6E_i(M2) + 6E_i(M3) + 6E_i(C)]}{20} \qquad (4.1)$$

whereas the cohesive energy (ΔE) can be expressed as:

$$\Delta E = \frac{E_{total} - [2E_s(M1) + 6E_s(M2) + 6E_s(M3) + 6E_s(C)]}{20} \qquad (4.2)$$

where E_{total} is the total energy of the M_7C_3 unit cell, $E_i(M)$ is the energy per atom of bulk M, $E_s(M)$ is the atomic energy of element M. The results are listed in Table 6. One may see that although replacing one Fe atom with W or V slightly influences the stability

of (Fe, Cr, X)$_7$C$_3$ negatively, the carbides are still stable as their formation energies and cohesive energies remain negative.

Table 6 - Formation energies and cohesive energies of Fe$_4$Cr$_3$C$_3$, Fe$_3$Cr$_3$WC$_3$ and Fe$_3$Cr$_3$VC$_3$

M1	M2	M3	ΔU (eV/atom)	ΔE (eV/atom)
Fe	Fe	Cr	-0.201	-8.772
W	Fe	Cr	-0.058	-6.049
V	Fe	Cr	-0.147	-5.839

4.2.4.2 Electron work function and mechanical properties of (Fe, Cr, X)$_7$C$_3$

The electron work function of pure metal decreases in a sequence of W, Fe, V. However, when the substitutional atom X replaces a Fe atom in Fe$_4$Cr$_3$C$_3$, whether the EWF of Fe$_3$Cr$_3$XC$_3$ would change in a similar trend as pure metal X remains unknown. The calculated work function of pure metal X and Fe$_3$Cr$_3$XC$_3$ are presented in Table 7, and the electron density maps of the (1 1 0) plane of three carbides are illustrated in Fig.25. According to the calculated results, using the substitute with higher EWF than Fe, such as W, would increase the EWF of corresponding carbides. As shown in Fig.25, the electron density between W and its surrounding atoms is increased, which indicates that W enhances the metallic bond and leads to higher EWF of carbides, whereas V shows an opposite effect.

Table 7 - Calculated EWF of elements and corresponding carbides

Element	W	Fe	V
EWF (eV)	4.412	4.247	4.139
Carbides	$Fe_3Cr_3WC_3$	$Fe_4Cr_3C_3$	$Fe_3Cr_3VC_3$
EWF (eV)	4.242	4.171	4.033
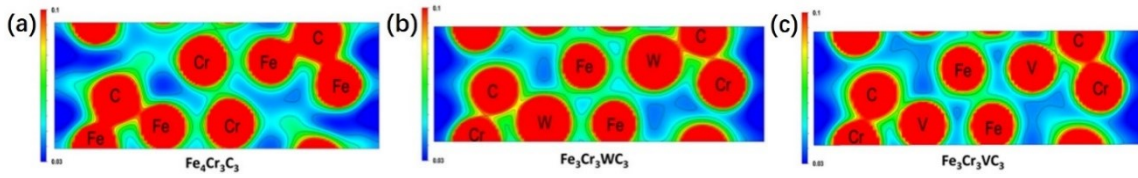
***Fig.25** Electron density distribution of (a) $Fe_4Cr_3C_3$, (b) $Fe_3Cr_3WC_3$ and (c) $Fe_3Cr_3VC_3$.*

The elastic matric of three carbides are then calculated and presented in Table 8. The mechanical properties, which are listed in Table 9, are derived from the following equations [111, 114]:

$$B_v = \frac{1}{9}[C_{11} + C_{22} + C_{33} + 2(C_{12} + C_{13} + C_{23})] \tag{4.3}$$

$$G_v = \frac{1}{15}[C_{11} + C_{22} + C_{33} + 3(C_{44} + C_{55} + C_{66}) - (C_{12} + C_{13} + C_{23})] \tag{4.4}$$

$$E = \frac{9B_v G_v}{3B_v + G_v} \tag{4.5}$$

Young's modulus of $Fe_3Cr_3WC_3$ is higher than $Fe_4Cr_3C_3$, while that of $Fe_3Cr_3VC_3$ is lower than $Fe_4Cr_3C_3$. The calculated moduli of carbides are consistent with the experimental observation. It also proves the hypothesis that in carbides, higher EWF

leads to enhanced mechanical strength. The value of B_v/G_v can be the criterion to determine whether a material is brittle or ductile [63]. When the B_v/G_v ratio is larger than 1.75, the material can be considered ductile. The higher the B_v/G_v ratio, the more flexible the material is. According to Table 9, with either W or V substitution, the flexibility of carbides increases. Therefore, one can say that the modification of M_7C_3 carbides with W may improve the mechanical properties of HCCIs since the mechanical strength and flexibility of M_7C_3 carbides are elevated simultaneously.

Table 8 - Calculated elastic constants C_{ij} of $Fe_4Cr_3C_3$, $Fe_3Cr_3WC_3$ and $Fe_3Cr_3VC_3$ (GPa)

	C_{11}	C_{12}	C_{13}	C_{22}	C_{23}	C_{33}	C_{44}	C_{55}	C_{66}
$Fe_4Cr_3C_3$	479.88	174.21	184.33	479.88	184.33	472.15	126.38	126.38	152.83
$Fe_3Cr_3WC_3$	495.92	211.76	220.42	495.92	220.42	450.55	144.59	144.59	142.08
$Fe_3Cr_3VC_3$	478.95	180.29	213.18	478.95	213.18	451.79	130.96	130.96	149.33

Table 9 - Calculated mechanical properties of $Fe_4Cr_3C_3$, $Fe_3Cr_3WC_3$ and $Fe_3Cr_3VC_3$ (GPa)

	B_v	G_v	B_v/G_v	E
$Fe_4Cr_3C_3$	279.74	140.39	1.99	360.81
$Fe_3Cr_3WC_3$	305.29	138.91	2.20	361.85
$Fe_3Cr_3VC_3$	291.44	136.38	2.14	353.93

4.3 Conclusions

1. W and V are soluble in M_7C_3 carbides and thus results in various EWF and Young's modulus of carbides.

2. From AFM measurements and first-principles calculations, the EWF of substitutional metal X is positively correlated to the EWF of corresponding $(Fe, Cr, X)_7C_3$ carbides.

3. The replacement of original atoms in M_7C_3 carbides with metallic substitute which has higher EWF would increase the electronic density and thus strengthen the metallic bonds. Hence, the mechanical strength of M_7C_3 is improved, which was proven by first-principles calculations and relevant experiments.

4. W-doped M_7C_3 exhibits not only enhanced mechanical strength, but also elevated flexibility.

Chapter 5 Conclusions

5.1 General conclusions

In this thesis, studies on the modification of primary carbides in hypereutectic HCCIs were conducted. Two ways, forming core-shell structured carbides promoted by boron addition and modifying mechanical properties of M_7C_3 with W and V addition, were investigated. Both studies were conducted with theoretical calculations as well as experimental validation.

1. According to the thermodynamics analysis, the compositional range to form core-shell structured carbides with B addition is expanded, which was verified by experimental observation. Also, the calculated driving force proves that $M_{23}(C, B)_6$ is stabilized with boron. The core-shell structured carbides are expected to improve the toughness of HCCIs containing a higher concentration of carbon and thus higher wear resistance.

2. Based on first-principles calculations, the formation energy of $M_{23}C_6$ decreases as boron is added. The mechanical strength and flexibility of $M_{23}C_6$ increase with one carbon atom replaced by boron.

3. Tungsten and vanadium were experimentally validated to be soluble in primary M_7C_3 and varied the EWF and mechanical properties of M_7C_3. The $(Fe, Cr, W)_7C_3$ carbide exhibits simultaneously increased Young's modulus and flexibility.

4. EWF of $(Fe, Cr, X)_7C_3$ has a positive correlation with the EWF of the substitute element X.

5. As EWF increases, the metallic bond becomes stronger, which leads to improved mechanical strength. Thus, one may say that EWF can be a promising indicator of the mechanical strength of materials.

5.2 Future work

1. Add metallic alloying elements such as Ti, W and V in HCCIs to promote the formation of core-shell structured carbides.

2. Investigate the mechanism of metallic elements promoting the formation of core-shell structured carbides and compare it with the mechanism of boron's promoting effect.

3. Design various types of carbides with different alloying elements to further prove the correlation of electron work function and Young's modulus.

Bibliography

[1] M. Jones, R.J. Llewellyn, Erosion–corrosion assessment of materials for use in the resources industry, Wear. 267 (2009) 2003-2009.

[2] L. Lu, H. Soda, A. McLean, Microstructure and mechanical properties of Fe–Cr–C eutectic composites, Materials Science and Engineering: A. 347 (2003) 214-222.

[3] R.J. Llewellyn, S.K. Yick, K.F. Dolman, Scouring erosion resistance of metallic materials used in slurry pump service, Wear. 256 (2004) 592-599.

[4] ÖN. Doğan, J.A. Hawk, G. Laird, Solidification structure and abrasion resistance of high chromium white irons, Metallurgical and Materials Transactions A. 28 (1997) 1315-1328.

[5] A. Wiengmoon, T. Chairuangsri, J.T.H. Pearce, A Microstructural Study of Destabilised 30wt%Cr-2.3wt%C High Chromium Cast Iron, ISIJ Int. 44 (2004) 396-403.

[6] J. Cui, L. Guo, H. Lu, D.Y. Li, Understanding effects of Cr content on the slurry erosion behavior of high-Cr cast irons through local property mapping and computational analysis, Wear. 376-377 (2017) 587-594.

[7] X.H. Tang, L. Li, B. Hinckley, K. Dolman, L. Parent, D.Y. Li, Beneficial Effects of the Core–Shell Structure of Primary Carbides in High-Cr (45 wt%) White Cast Irons on Their Mechanical Behavior and Wear Resistance, Tribology Letters. 58 (2015) 44.

[8] X. Wu, J. Xing, H. Fu, X. Zhi, Effect of titanium on the morphology of primary M7C3 carbides in hypereutectic high chromium white iron, Materials Science and Engineering: A. 457 (2007) 180-185.

[9] T.Z. Li, L. Li, H. Lu, L. Parent, H. Tian, R.J. Chung, D.Y. Li, Effect of trace Ni on the resistance of high-Cr cast iron to slurry erosion, Wear. 426-427 (2019) 605-611.

[10] J.T.H. Pearce, D.W.L. Elwell, Duplex nature of eutectic carbides in heat treated 30% chromium cast iron, J. Mater. Sci. Lett. 5 (1986) 1063-1064.

[11] A. Inoue, T. Masumoto, Carbide reactions (M3C→M7C3→M23C6→M6C) during tempering of rapidly solidified high carbon Cr-W and Cr-Mo steels, Metallurgical Transactions A. 11 (1980) 739-747.

[12] J. Cui, H. Guo, J.W. Li, D.Y. Li, L. Parent, H. Tian, A computational study on the benefit of core-shell structured carbides to the erosion resistance of high-Cr cast irons, Tribology International. 103 (2016) 432-439.

[13] K. Wang, D. Li, Formation of core (M7C3)-shell (M23C6) structured carbides in white cast irons: A thermo-kinetic analysis, Computational Materials Science. 154 (2018) 111-121.

[14] N. Yüksel, S. Şahin, Wear behavior–hardness–microstructure relation of Fe–Cr–C and Fe–Cr–C–B based hardfacing alloys, Materials & Design. 58 (2014) 491-498.

[15] R. Correa, A. Bedolla-Jacuinde, J. Zuno-Silva, E. Cardoso, I. Mejía, Effect of boron on the sliding wear of directionally solidified high-chromium white irons, Wear. 267 (2009) 495-504.

[16] J.W. Yoo, S.H. Lee, C.S. Yoon, S.J. Kim, The effect of boron on the wear behavior of iron-based hardfacing alloys for nuclear power plants valves, Journal of Nuclear Materials. 352 (2006) 90-96.

[17] I.R. Shein, N.I. Medvedeva, A.L. Ivanovskii, Electronic and structural properties of cementite-type M3X (M=Fe, Co, Ni; X=C or B) by first principles calculations, Physica B: Condensed Matter. 371 (2006) 126-132.

[18] H. Lu, T. Li, J. Cui, Q. Li, D.Y. Li, Improvement in erosion-corrosion resistance of high-chromium cast irons by trace boron, Wear. 376-377 (2017) 578-586.

[19] S.M. Tomovic-Petrovic, S.V. Markovic, S. Zec, The effect of boron on the amount and type of carbides in chromium white irons, J. Serb. Chem. Soc. 67 (2002) 697-707.

[20] R. Sahara, T. Matsunaga, H. Hongo, M. Tabuchi, Theoretical Investigation of Stabilizing Mechanism by Boron in Body-Centered Cubic Iron Through (Fe,Cr)23(C,B)6 Precipitates, Metallurgical and Materials Transactions A. 47 (2016) 2487-2497.

[21] A. Röttger, J. Lentz, W. Theisen, Boron-alloyed Fe–Cr–C–B tool steels — Thermodynamic calculations and experimental validation, Materials & Design. 88 (2015) 420-429.

[22] J. Lentz, A. Röttger, W. Theisen, Mechanism of the Fe3(B,C) and Fe23(C,B)6 solid-state transformation in the hypoeutectic region of the Fe-C-B system, Acta Materialia. 119 (2016) 80-91.

[23] X. Chong, M. Hu, P. Wu, Q. Shan, Y.H. Jiang, Z.L. Li, J. Feng, Tailoring the anisotropic mechanical properties of hexagonal M7X3 (M=Fe, Cr, W, Mo; X=C, B) by multialloying, Acta Materialia. 169 (2019) 193-208.

[24] K. Yamamoto, S. Inthidech, N. Sasaguri, Y. Matsubara, Influence of Mo and W on High Temperature Hardness of M7C3 Carbide in High Chromium White Cast Iron, MATERIALS TRANSACTIONS. 55 (2014) 684-689.

[25] G. Hua, D. Li, Generic relation between the electron work function and Young's modulus of metals, Appl. Phys. Lett. 99 (2011) 041907.

[26] G. Hua, D. Li, The correlation between the electron work function and yield strength of metals, Phys. Status Solidi B. 249 (2012) 1517-1520.

[27] G. Hua, D. Li, Electron work function: a novel probe for toughness, Phys. Chem. Chem. Phys. 18 (2016) 4753-4759.

[28] A. Wiengmoon, Carbides in high chromium cast irons, Naresuan University Engineering Journal. 6 (2011) 64-71.

[29] Alloy Cast Irons, in: J.R. Davis (Ed.), Metals Handbook Desk Edition, ASM International, 1998, pp. 0.

[30] K. Ogi, Y. Matsubara, K. Matsuda, Eutectic Solidification of High-Chromium Cast Iron--Mechanism of Eutectic Growth, American Foundrymen's Society, Transactions. 89 (1981) 197-204.

[31] Y. Sentarli, Suspension casting of a high chromium white iron.

[32] J.K. Fulcher, T.H. Kosel, N.F. Fiore, The effect of carbide volume fraction on the low stress abrasion resistance of high Cr-Mo white cast irons, Wear. 84 (1983) 313-325.

[33] K. Zum Gahr, G.T. Eldis, Abrasive wear of white cast irons, Wear. 64 (1980) 175-194.

[34] J. Pearce, Abrasive wear behaviour of alloy cast irons, Br.Foundryman. 78 (1985) 13-23.

[35] E. Hornbogen, J.M. Motz, Fracture toughness of gray cast irons, INTERNATIONAL CAST METALS JOURNAL. 2 (1977) 31-36.

[36] K.Z. Gahr, Bruchzähigkeit von Härtungsgefügen des Werkzeugstahls 90 MnCrV 8, Archiv für das Eisenhüttenwesen. 49 (1978) 581-586.

[37] ÖN. Doğan, J.A. Hawk, G. Laird, Solidification structure and abrasion resistance of high chromium white irons, Metallurgical and Materials Transactions A. 28 (1997) 1315-1328.

[38] C.P. Tabrett, I.R. Sare, M.R. Ghomashchi, Microstructure-property relationships in high chromium white iron alloys, International Materials Reviews. 41 (1996) 59-82.

[39] ÖN. Doğan, G. Laird II, J.A. Hawk, Abrasion resistance of the columnar zone in high Cr white cast irons, Wear. 181 (1995) 342-349.

[40] J.D. Watson, P.J. Mutton, I.R. Sare, Abrasive wear of white cast irons, (1980).

[41] J.J. Coronado, Effect of (Fe, Cr) 7C3 carbide orientation on abrasion wear resistance and fracture toughness. Wear 270 (2011) 287-293.

[42] D. Li, Abrasive Wear, in: G.E. Totten (Ed.), Friction, Lubrication, and Wear Technology, ASM International, 2017, pp. 0.

[43] Chapter 11 - Abrasive, Erosive and Cavitation Wear, Engineering Tribology (Fourth Edition). (2014) 525-576.

[44] S.G. Sapate, A.V. Rama Rao, Effect of carbide volume fraction on erosive wear behaviour of hardfacing cast irons, Wear. 256 (2004) 774-786.

[45] A.N.J. Stevenson, I.M. Hutchings, Wear of hardfacing white cast irons by solid particle erosion, Wear. 186-187 (1995) 150-158.

[46] S. Chatterjee, T.K. Pal, Solid particle erosion behaviour of hardfacing deposits on cast iron—Influence of deposit microstructure and erodent particles, Wear. 261 (2006) 1069-1079.

[47] J.T.H. Pearce, D.W.L. Elwell, Duplex nature of eutectic carbides in heat treated 30% chromium cast iron, J. Mater. Sci. Lett. 5 (1986) 1063-1064.

[48] K. Wieczerzak, P. Bala, R. Dziurka, T. Tokarski, G. Cios, T. Koziel, L. Gondek, The effect of temperature on the evolution of eutectic carbides and $M_7C_3 \rightarrow M_{23}C_6$ carbides reaction in the rapidly solidified Fe-Cr-C alloy, Journal of Alloys and Compounds. 698 (2017) 673-684.

[49] J.T.H. Pearce, High chromium cast irons to resist abrasive wear, Foundryman. 95 (2002) 156-166.

[50] X. Zhi, J. Liu, J. Xing, S. Ma, Effect of cerium modification on microstructure and properties of hypereutectic high chromium cast iron, Materials Science and Engineering: A. 603 (2014) 98-103.

[51] L.E. Eiselstein, O.A. Ruano, O.D. Sherby, Structural characterization of rapidly solidified white cast iron powders, J. Mater. Sci. 18 (1983) 483-492.

[52] K.H.W. Seah, J. Hemanth, S.C. Sharma, Wear characteristics of sub-zero chilled cast iron, Wear. 192 (1996) 134-140.

[53] G. Laird II, Microstructures of Ni-hard I, Ni-hard IV and high-Cr white cast irons, AFS Transactions. 99 (1991) 339-357.

[54] Q. Li, Stress analysis of large columnar oil tank on flexible foundation, Pet. Refin. Eng. 32 (2002) 56-59.

[55] M. Qian, W. Chaochang, S. Harada, Modification of hypoeutectic low alloy white cast irons, J. Mater. Sci. 31 (1996) 1865-1871.

[56] M.M. Arikan, H. ÷imenoglu, E.S. Kayali, Effect of titanium on the abrasion resistance of 15Cr-3Mo white cast iron, Wear. 247 (2001) 231-235.

[57] A. Bedolla-Jacuinde, R. Correa, J.G. Quezada, C. Maldonado, Effect of titanium on the as-cast microstructure of a 16%chromium white iron, Mater. Sci. Eng. A. 398 (2005) 297-308.

[58] Q.X. Yang, Y.W. Gao, B. Liao, M. Yao, Discussion of inclusions as heterogeneous nuclei of primary austenite of medium-high carbon steel during hardfacing, J.Rare Earths. 18 (2000) 138-141.

[59] G.Y. Liang, J.Y. Su, The effect of rare earth elements on the growth of eutectic carbides in white cast irons containing chromium, Cast Metals. 4 (1991) 83-88.

[60] X. Zhi, J. Xing, Y. Gao, H. Fu, J. Peng, B. Xiao, Effect of heat treatment on microstructure and mechanical properties of a Ti-bearing hypereutectic high chromium white cast iron, Mater. Sci. Eng. A. 487 (2008) 171-179.

[61] Q. Liu, P. Hedström, H. Zhang, Q. Wang, P.G. Jönsson, K. Nakajima, Effect of heat treatment on microstructure and mechanical properties of Ti-alloyed hypereutectic high chromium cast iron, ISIJ Int. 52 (2012) 2288-2294.

[62] X. Qi, Z. Jia, Q. Yang, Y. Yang, Effects of vanadium additive on structure property and tribological performance of high chromium cast iron hardfacing metal, Surface and Coatings Technology. 205 (2011) 5510-5514.

[63] S. Liu, Y. Zhou, X. Xing, J. Wang, Q. Yang, Refining effect of TiC on primary M7C3 in hypereutectic FeCrC harden-surface welding coating: Experimental research and first-principles calculation, Journal of Alloys and Compounds. 691 (2017) 239-249.

[64] S. Liu, Z. Wang, Z. Shi, Y. Zhou, Q. Yang, Experiments and calculations on refining mechanism of NbC on primary M7C3 carbide in hypereutectic Fe-Cr-C alloy, Journal of Alloys and Compounds. 713 (2017) 108-118.

[65] X. Zhi, J. Xing, H. Fu, B. Xiao, Effect of niobium on the as-cast microstructure of hypereutectic high chromium cast iron, Materials Letters. 62 (2008) 857-860.

[66] D. Turnbull, B. Vonnegut, Nucleation Catalysis, Ind. Eng. Chem. 44 (1952) 1292-1298.

[67] B.L. Bramfitt, The effect of carbide and nitride additions on the heterogeneous nucleation behavior of liquid iron, MT. 1 (1970) 1987-1995.

[68] R.K. Galgali, H.S. Ray, A.K. Chakrabarti, Wear characteristics of TiC reinforced cast iron composites. Part 1 - Adhesive wear, Mater. Sci. Technol. 14 (1998) 810-815.

[69] C.C. Degnan, P.H. Shipway, J.V. Wood, Elevated temperature sliding wear behaviour of TiC-reinforced steel matrix composites, Wear. 250-251 (2001) 1444-1451.

[70] Z. Mei, Y.W. Yan, K. Cui, Effect of matrix composition on the microstructure of in situ synthesized TiC particulate reinforced iron-based composites, Mater Lett. 57 (2003) 3175-3181.

[71] L. Contreras, X. Turrillas, M.J. Mas-Guindal, G.B.M. Vaughan, Å Kvick, M.A. Rodríguez, Synchrotron diffraction studies of TiC/FeTi cermets obtained by SHS, J. Solid State Chem. 178 (2005) 1595-1600.

[72] H.C. Eckstrom, W.A. Adcock, A new iron carbide in hydrocarbon synthesis catalysts, J. Am. Chem. Soc. 72 (1950) 1042-1043.

[73] Y. Qu, J. Xing, X. Zhi, J. Peng, H. Fu, Effect of cerium on the as-cast microstructure of a hypereutectic high chromium cast iron, Materials Letters. 62 (2008) 3024-3027.

[74] P. Zhang, Y. Zhou, J. Yang, D. Li, X. Ren, Y. Yang, Q. Yang, Optimization on mechanical properties of $Fe_{7-x}Cr_xC_3$ carbides by first-principles investigation, Journal of Alloys and Compounds. 560 (2013) 49-53.

[75] Chapter 3 - Basic Thermodynamics, Pergamon Materials Series. 1 (1998) 33-57.

[76] Chapter 5 - Thermodynamic Models for Solution and Compound Phases, Pergamon Materials Series. 1 (1998) 91-126.

[77] J. Tcheska, Discussion of approximation formulas for thermodynamic excess functions with special regard to best fit of mass spectrometric data on medal alloys, Calphad. 4 (1980) 63-81.

[78] Chapter 9 - Computational Methods, Pergamon Materials Series. 1 (1998) 261-296.

[79] L. Kaufman, H. Bernstein, Computer calculation of phase diagrams. With special reference to refractory metals, (1970).

[80] W.B. White, S.M. Johnson, G.B. Dantzig, Chemical equilibrium in complex mixtures, J. Chem. Phys. 28 (1958) 751-755.

[81] G. Eriksson, Thermodynamic Studies of High Temperature Equilibria, Chem.Scr. 8 (1975) 100-103.

[82] B. Jansson, A General Method for Calculating Phase Equilibria Under Different Types of Conditions. 1984.

[83] A.T. Dinsdale, S.M. Hodson, T.I. Barry, J.R. Taylor, COMPUTATIONS USING MTDATA OF METAL - MATTE - SLAG - GAS EQUILIBRIA, Proceedings of the International Symposium on Computer Software in Chemical and Extractive Metallurgy. (1989) 59-74.

[84] H.L. Lukas, E.T. Henig, B. Zimmermann, Optimization of phase diagrams by a least square's method using simultaneously different types of data, Calphad. 1 (1977) 225-236.

[85] D.W. Marquardt, An algorithm for least-squares estimation of nonlinear parameters, Journal of the society for Industrial and Applied Mathematics. 11 (1963) 431-441.

[86] B. Jansson, Evaluation of Parameters in Thermochemical Models using Different Types of Experimental Data Simultaneously, 1984.

[87] M.J.D. Powell, A Method for Minimizing a Sum of Squares of Non-Linear Functions Without Calculating Derivatives, comjnl. 7 (1965) 303-307.

[88] N. Pervaiz, I. Aziz, Haar wavelet approximation for the solution of cubic nonlinear Schrodinger equations, Physica A: Statistical Mechanics and its Applications. (2019) 123738.

[89] E. Schrödinger, Quantisierung als Eigenwertproblem, Ann. Phys. 384 (1926) 361-376.

[90] R. Jost, A. Pais, On the Scattering of a Particle by a Static Potential, Phys. Rev. 82 (1951) 840-851.

[91] M. Born, V. Fock, Beweis des Adiabatensatzes, Zeitschrift für Physik. 51 (1928) 165-180.

[92] P. Hohenberg, W. Kohn, Inhomogeneous electron gas, Physical review. 136 (1964) B864.

[93] W. Kohn, L.J. Sham, Self-Consistent Equations Including Exchange and Correlation Effects, Phys. Rev. 140 (1965) A1133-A1138.

[94] A. Zupan, P. Blaha, K. Schwarz, J.P. Perdew, Pressure-induced phase transitions in solid Si, SiO 2, and Fe: Performance of local-spin-density and generalized-gradient-approximation density functionals, Physical Review B. 58 (1998) 11266.

[95] J.C. Grossman, L. Mitas, K. Raghavachari, Structure and stability of molecular carbon: importance of electron correlation, Phys. Rev. Lett. 75 (1995) 3870.

[96] D. Johnson, N. Hilal, W.R. Bowen, Chapter 1 - Basic Principles of Atomic Force Microscopy, Atomic Force Microscopy in Process Engineering. (2009) 1-30.

[97] V. Bellitto, Atomic Force Microscopy: Imaging, Measuring and Manipulating Surfaces at the Atomic Scale, BoD–Books on Demand, 2012.

[98] T. Okajima, H. Sekiguchi, H. Arakawa, A. Ikai, Self-oscillation technique for AFM in liquids, Appl. Surf. Sci. 210 (2003) 68-72.

[99] M. Kageshima, H. Jensenius, M. Dienwiebel, Y. Nakayama, H. Tokumoto, S.P. Jarvis, T.H. Oosterkamp, Noncontact atomic force microscopy in liquid environment with quartz tuning fork and carbon nanotube probe, Appl. Surf. Sci. 188 (2002) 440-444.

[100] Y. Song, B. Bhushan, Finite-element vibration analysis of tapping-mode atomic force microscopy in liquid, Ultramicroscopy. 107 (2007) 1095-1104.

[101] F.M. Zhang, X.C. Liu, J. Gao, X.S. Wu, Y.W. Du, H. Zhu, J.Q. Xiao, P. Chen, Investigation on the magnetic and electrical properties of crystalline $Mn_{0.05}Si_{0.95}$ films, Appl. Phys. Lett. 85 (2004) 786-788.

[102] G. Hübschen, I. Altpeter, R. Tschuncky, H. Herrmann, Materials Characterization using Nondestructive Evaluation (NDE) Methods, Woodhead publishing, 2016.

[103] Q. Zhong, D. Inniss, K. Kjoller, V.B. Elings, Fractured polymer/silica fiber surface studied by tapping mode atomic force microscopy, Surface Science Letters. 290 (1993) L688-L692.

[104] 4. Hansma, J.P. Cleveland, M. Radmacher, D.A. Walters, P.E. Hillner, M. Bezanilla, M. Fritz, D. Vie, H.G. Hansma, C.B. Prater, Tapping mode atomic force microscopy in liquids, Appl. Phys. Lett. 64 (1994) 1738-1740.

[105] H.G. Hansma, R.L. Sinsheimer, J. Groppe, T.C. Bruice, V. Elings, G. Gurley, M. Bezanilla, I.A. Mastrangelo, P.V. Hough, P.K. Hansma, Recent advances in atomic force microscopy of DNA, Scanning. 15 (1993) 296-299.

[106] J. Andersson, T. Helander, L. Höglund, P. Shi, B. Sundman, Thermo-Calc & DICTRA, computational tools for materials science, Calphad. 26 (2002) 273-312.

[107] G. Kresse, J. Furthmüller, Efficient iterative schemes for ab initio total-energy calculations using a plane-wave basis set, Phys. Rev. B Condens. Matter Mater. Phys. 54 (1996) 11169-11186.

[108] G. Kresse, J. Hafner, Ab initio molecular dynamics for liquid metals, Physical Review B. 47 (1993) 558-561.

[109] J.P. Perdew, K. Burke, M. Ernzerhof, Generalized gradient approximation made simple, Phys. Rev. Lett. 77 (1996) 3865-3868.

[110] J.J. Han, C.P. Wang, X.J. Liu, Y. Wang, Z.-. Liu, First-principles calculation of structural, mechanical, magnetic and thermodynamic properties for γ-M23C6 (M = Fe, Cr) compounds, J Phys Condens Matter. 24 (2012).

[111] Z. Wu, E. Zhao, H. Xiang, X. Hao, X. Liu, J. Meng, Crystal structures and elastic properties of superhard IrN_ {2} and IrN_ {3} from first principles, Phys. Rev. B. 76 (2007).

[112] A. Kipelova, A. Belyakov, R. Kaibyshev, The crystallography of M23C6 carbides in a martensitic 9% Cr steel after tempering, aging and creep, Philosophical Magazine. 93 (2013) 2259-2268.

[113] L. Wang, K.C. Lai, L. Huang, J.W. Evans, Y. Han, Low-index surface energies, cleavage energies, and surface relaxations for crystalline NiAl from first-principles calculations, Surface Science. (2019) 121532.

[114] Y. Tian, B. Xu, Z. Zhao, Microscopic theory of hardness and design of novel superhard crystals, International Journal of Refractory Metals and Hard Materials. 33 (2012) 93-106.